A mathematical model of osteocyte network control of bone mechanical adaptation

Adel Mehrpooya[a], Vivien J Challis[a], Pascal R Buenzli[a,*]

[a]School of Mathematical Sciences, Queensland University of Technology (QUT), Brisbane, Australia

October 10, 2025

Abstract

The osteocyte network embedded in bone tissues plays a central role in the control of bone adaptation to mechanical loads and micro-damage repair. However, much remains to be understood about the precise mechanisms by which the osteocyte network regulates bone formation and bone resorption based on the propagation of biochemical signals emitted in response to mechanical stimulus. In this work, we propose a simple one-dimensional computational model of bone mechanical adaptation based on the propagation of signalling molecules through a dynamic osteocyte network. The osteocyte network is extended during bone formation, and reduced during bone resorption, which affects the generation and propagation of the signalling molecules to the bone surface. We explore how this osteocyte-based model of bone mechanosensation and mechanoresponse gives rise to effective Wolff's laws, in which overloaded bone is consolidated and underloaded bone is removed. We find that the pointwise addition and removal of osteocytes significantly affects signalling molecules propagating to the bone surface, which in turn affects the dynamics of bone formation and bone resorption. The explicit consideration of signal propagation through a dynamic network leads to new behaviours compared to previous models, such as partial bone recovery after an unloading and reloading cycle, and a minimum loading threshold below which all bone is resorbed when osteocytes are stimulated by mechanical stress (but not when they are stimulated by the strain energy density). While many extensions of this mathematical model are possible, it provides a first illustration of how the osteocyte network can act as a dynamic embedded control network for bone adaptation to mechanical loads.

Key words: Mechanical loading, Bone remodelling, Signal propagation, Wolff's law, Reaction-diffusion model

1 Introduction

Bone is an adaptive biological tissue that fulfills important mechanical functions (Martin, Burr & Sharkey 1998; Cowin 2001). To be light and strong, bone optimises its shape in response to mechanical loading, such that regions experiencing high loads are consolidated and regions experiencing low loads are removed (Bertram & Swartz 1991; Turner 1999; Hernandez, Carter & Beaupré 2000; Carter & Beaupré 2001; Frost 2003; Skerry 2008; Rosa et al. 2015). Bone tissues also undergo continual self-repair to prevent the accumulation of fatigue micro-cracks (Martin 2003). Old, damaged tissue is periodically replaced with new tissue by a process called

[1]Corresponding author. Email address: `pascal.buenzli@qut.edu.au`

bone remodelling. Bone adaptation and bone remodelling are fundamental biological processes that allow our bones to be mechanically under-engineered without risking spontaneous fracture (Martin 2003).

There is increasing evidence that the osteocyte network embedded in bone tissue is central to the orchestration and control of these adaptative processes (Mullender et al. 1996; Qiu et al. 2002a,b; Vashishth et al. 2000; Tiede-Lewis & Dallas 2019). Osteocytes are mechanosensitive cells that live within a fluid-filled porous network called the lacunocanalicular network (LCN) (Buenzli & Sims 2015). These cells can respond to mechanical stimulation by emitting signalling molecules, such as sclerostin and RANKL (Turner & Forwood 1995; Knothe Tate et al. 2000; Robling, Castillo & Turner 2006; Ryser Nigam & Komarova; Nakashima et al. 2011; Moriishi et al. 2012; van Tol et al. 2020a,b). The presence of osteocytes within hard bone tissue enables these cells to identify regions needing consolidation, removal, or repair. Signals emitted by osteocytes in response to mechanical stimulation propagate through the LCN or through cell–cell connections to the bone surface, where they can promote the generation of osteoblasts (bone-forming cells) or osteoclasts (bone-resorbing cells) (Bonewald 2011; Franz-Odendaal, Hall & Witten 2006; Marotti 2000; Palumbo & Ferretti 2021; Ferretti & Palumbo 2021).

Many computational models of bone adapation to mechanical loading are based on Wolff's law (Huiskes et al. 1987; Mullender et al. 1995; Carter & Beaupré 2001; Jang & Kim 2010; Schulte et al. 2013; Wang et al. 2020, 2023). These models are successfully used in orthodontics and orthopaedics to predict the stability of screws and implants (Chou, Jagodnik & Müftü 2008; Ferguson et al. 2022; Wan et al. 2022) and to simulate changes in the shape and microstructure of bone subjected to physical loads (Mullender et al. 1995; Jang & Kim 2010; Adachi et al. 2010; Farhoudi et al. 2017; Fallahnezhad et al. 2017). Such models may be coupled with pharmacokinetic models to simulate osteoporosis therapies targeting osteocytes (Joerg et al. 2022). These computational models usually assume a fixed reference mechanical state, called the mechanical setpoint. Few studies investigate links between the cellular network of osteocytes and bone's ability to sense and respond to mechanics (Lerebours & Buenzli 2016; Pauchard & Buenzli 2025). While some works include osteocyte signalling in bone adaptation models (Mullender et al. 1995; van Oers et al. 2008; Adachi et al. 2010), they do not account for the fact that the osteocyte network itself is dynamic due to bone formation and resorption, which influences how signals propagate through the network to the bone surface. How the osteocyte network acts as a regulatory network for bone adaptation while itself being affected by adaptation is an important question that mathematical modelling can help answer.

In this work, we propose a simple one-dimensional computational model of bone mechanical adaptation based on the propagation of signalling molecules through a dynamic osteocyte network. The molecules are emitted by osteocytes in response to mechanical stimulation. They propagate to the bone surface, where they induce the formation of osteoblasts (bone-forming cells) or osteoclasts (bone-resorbing cells). The osteocyte network is extended during bone formation, and reduced during bone resorption. These processes affect the generation and propagation of the signalling molecules. We explore how this osteocyte-based model of bone mechanosensation and mechanoresponse gives rise to effective Wolff's laws, in which overloaded bone is consolidated and underloaded bone is removed. The aim of our study is to use this simple model of signal propagation to analyse qualitatively (i) how osteocyte regulation of bone formation and resorption affects the extent and propagation properties of the osteocyte network itself; (ii) how mechanical adaptation depends on the type of mechanical stimulus assumed to trigger osteocyte responses; and (iii) how osteoblasts and osteoclasts may respond to signals emanating from the network's edges at the bone surfaces. Our model builds on our previous work of signal propagation through (static) one-dimensional spatial networks using stochastic and

deterministic random walks and their continuum limit (Mehrpooya, Challis & Buenzli 2024). While the model we propose represents a simplified view of bone mechanical adaptation, it reveals useful insights into processes underlying bone mechanosensation and mechanoresponse that provide a first illustration of how the osteocyte network acts as a regulatory embedded control network.

2 Mathematical Model

2.1 Signal propagation in the osteocyte network

In this section we present a model of the propagation of signalling molecules within a one-dimensional, dynamic osteocyte network embedded in bone tissue. This model is based on the random walk model proposed by Mehrpooya, Challis & Buenzli (2024), however we restrict the current work to a deterministic model and do not consider stochasticity. The network can be considered to represent the osteocyte network in a one-dimensional slice $b_-(t) \leqslant x \leqslant b_+(t)$ through the cortical wall of a mouse tibia, where the position of the left bone boundary $b_-(t)$ and the right bone boundary $b_+(t)$ can vary with time t, as shown schematically in Figure 1.

Our focus is on the adaptation of bone via the time-evolution of bone boundaries regulated by the osteocyte network. The network is assumed to be represented by regularly spaced osteocytes with spacing Δx. Each osteocyte is labelled by a discrete index $i = i_-, i_-+1, \ldots, i_+-1, i_+$ and is located at position $x_i = i\Delta x$ (Figure 1b). We denote by i_- the index of the left-most osteocyte at time t, and by i_+ the index of the right-most osteocyte at time t. These indices depend on time due to the dynamic population of osteocytes, see Section 2.2.

We denote the quantity of signalling molecules positioned at osteocyte i at time t by $N_i(t)$ (Figure 1b). Molecules are assumed to be generated by osteocytes in response to a mechanical stimulus. The rate of molecule production at osteocyte i is denoted by $R(x_i, t, N_i)$ (number per unit time). Signalling molecules are also assumed to propagate to neighbouring osteocytes. We define q_i^{-1}, q_i^1 and q_i^0 as the fractions of molecules that move left, right, or remain stationary at osteocyte i, respectively, during the time interval Δt. These fractions are such that $q_i^{-1} + q_i^0 + q_i^1 = 1$. While longer-range jumps could be considered, representative signalling behaviour occurs when including only these nearest-neighbour jumps (Mehrpooya, Challis & Buenzli 2024). With the above notation, the evolution of the molecular occupancy is described by the update rule

$$N_i(t+\Delta t) = q_{i-1}^1 N_{i-1}(t) + q_{i+1}^{-1} N_{i+1}(t) + q_i^0 N_i(t) + R(x_i, t, N_i)\Delta t. \tag{1}$$

This update rule applies for $i_- \leqslant i \leqslant i_+$ with the convention that $q_{i_--1}^1 = 0$ and $q_{i_++1}^{-1} = 0$, meaning that molecules can jump out of the network at the left and right bone boundaries, but not re-enter the network. This represents absorbing boundary conditions and the fact that signalling molecules coming out of the osteocyte network are processed by the micro-environment to induce bone formation or bone resorption. The flux of molecules coming out of the bone surface at the left and right boundaries of the network (number per unit time) is given by

$$J_-(t) = \frac{N_-(t) - N_-(t-\Delta t)}{\Delta t} \quad \text{and} \quad J_+(t) = \frac{N_+(t) - N_+(t-\Delta t)}{\Delta t}, \tag{2}$$

where $N_-(t)$ and $N_+(t)$ are the cumulative numbers of molecules that jump out of the network up until time t at the left and right boundary, respectively. These numbers include molecules jumping out of the network by Eq. (1), and molecules released into the microenvironment by resorption of the left-most or right-most osteocyte (see Section 2.2).

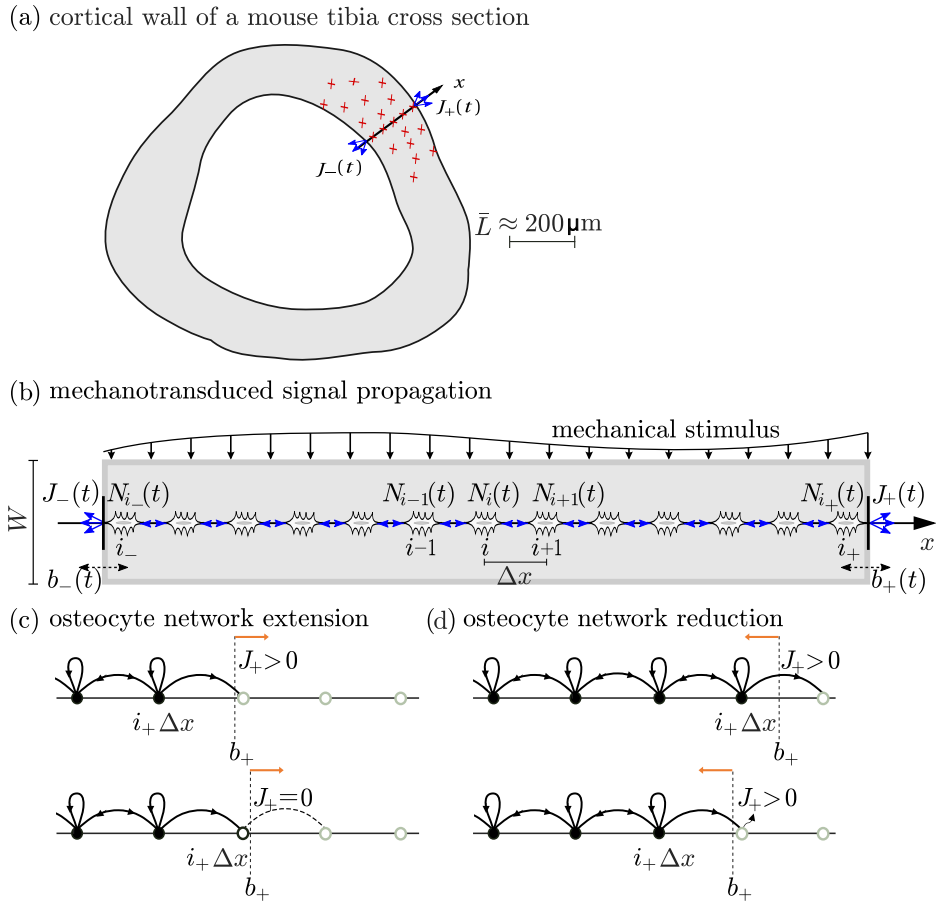

Figure 1 – (a) Two-dimensional cross-section of a mouse tibia cortical wall (grey) showing the x-axis as a slice across the cortical wall. Osteocytes (red pluses) along this axis emit and propagate signalling molecule to the bone surface, where they induce signalling fluxes $J_-(t)$ and $J_+(t)$. (b) Osteocytes are placed at equal distance Δx from each other along x. The ith osteocyte has a number of signalling molecules $N_i(t)$. The slice is assumed to be stimulated mechanically by a space and time-dependent loading force. Signalling molecules propagate between osteocytes until they reach the bone boundaries $b_\pm(t)$. The fluxes $J_\pm(t)$ of signalling molecules emanating from the bone surface induce bone formation or bone resorption. (c) Evolution of the osteocyte network during bone formation. Before the network extends (top), the flux $J_+ > J_0$. When a new osteocyte is formed (bottom), it is initialised with zero signalling molecules, so $J_+ = 0$. (d) Evolution of the osteocyte network during bone resorption. Before the network reduces (top), the flux $J_+ < J_0$ is due to molecules jumping right from the rightmost osteocyte. When an osteocyte is removed (bottom), the flux J_+ accounts for molecules jumping right from the new right-most osteocytes and molecules that were previously in the resorbed osteocyte.

Osteocytes may respond to a variety of mechanical stimulations. We propose a simple mechanotransduction model in which the more mechanically stimulated osteocytes are, the more they produce signalling molecules. We consider two models for the molecule production rate $R(x_i, t, N_i)$ in Eq. (1). The first assumes that osteocytes are stimulated by mechanical stress, such that the production of signalling molecules is

$$R_\sigma(x,t,N) = \lambda_1 \frac{\sigma(x,t)}{\overline{\sigma}} - \lambda_2 N, \tag{3}$$

where $\sigma(x,t)$ denotes the mechanical stress at position x and time t, $\overline{\sigma}$ denotes a reference

stress, and $\lambda_1 > 0$ (day^{-1}) and $\lambda_2 > 0$ (day^{-1}) are rates of molecule production and degradation, respectively. The stress is computed as force per unit area using

$$\sigma(x,t) = \frac{F(x,t)}{L(t)W}, \tag{4}$$

where $F(x,t)$ is the applied mechanical force on the bone slice at position x and time t, $L(t) = b_+(t) - b_-(t)$ is the cortical wall thickness, and $W = 20\,\mu\text{m}$ is the assumed distance between osteocytes in the lateral direction (Qin et al. 2020) (see Figure 1(b)). The choice of W affects the scale of the appropriate force F to apply but is otherwise irrelevant.

Our second mechanotransduction model considers that osteocytes are stimulated by the strain energy density, such that the production rate of signalling molecules is

$$R_\Psi(x,t,N) = \lambda_1 \frac{\Psi(x,t)}{\overline{\Psi}} - \lambda_2 N, \tag{5}$$

where $\Psi(x,t)$ is the strain energy density and $\overline{\Psi}$ denotes a reference strain energy density. The strain energy density can be computed as

$$\Psi(x,t) = \frac{1}{2}\varepsilon\sigma = \frac{1}{2E}\sigma^2 = \frac{1}{2E}\left(\frac{F(x,t)}{WL(t)}\right)^2. \tag{6}$$

Here, ε is the strain and E is Young's modulus. These quantities are related to the stress σ via Hooke's law $\sigma = E\varepsilon$.

To determine reference values for the above mechanics-related parameters, we use data from the literature. These values are summarised in Table 1. We take the reference cortical wall width of a mouse tibia to be $\overline{L} = 200\,\mu\text{m}$, consisting of 21 osteocytes spaced at intervals of $\Delta x = 10\,\mu\text{m}$ (van Tol et al. 2020a; Mehrpooya, Challis & Buenzli 2024). The Young's modulus of a mouse tibia is typically reported as ranging between 10 GPa and 15 GPa (Oliviero et al. 2021), and we take a value of $E = 10$ GPa. With this value of E and a reference strain value of $10^3\,\mu\varepsilon$ (microstrains), we obtain a reference stress value of $\overline{\sigma} = 10$ MPa, which is reasonable for a mouse tibia (van Tol et al. 2020a). From Eq. (4), the value of the force that gives a stress of $\overline{\sigma}$ is therefore

$$\overline{F} = \overline{\sigma}\,\overline{L}W = 0.04\,\text{N}. \tag{7}$$

The same reference force applies in the case of Eq. (5), with $\overline{\Psi} = 5 \times 10^3$ MPa computed from Eq. (6) using E and $\overline{\sigma}$.

It will be useful to consider the continuum limit of this discrete model of signalling molecule propagation. To this effect, we introduce the concentration $n_i(t)$ of molecules at osteocyte i at time t, given by

$$n_i(t) = \frac{N_i(t)}{\Delta x}. \tag{8}$$

In Mehrpooya, Challis & Buenzli (2024), we showed that in the limit where Δt and Δx approach zero, Eq. (1) converges to the following reaction–advection–diffusion equation:

$$\frac{\partial n}{\partial t} = -\frac{\partial}{\partial x}\left(\upsilon n - D\frac{\partial}{\partial x}\right) + \rho R\left(x,t,\frac{n(x,t)}{\rho}\right), \tag{9}$$

where $n(x,t)$ represents the concentration of signalling molecules at position x and time t, such that $n(x_i,t) = n_i(t)$. In Eq. (9), $\rho = 1/\Delta x$ is the osteocyte density, D is the diffusivity and

v is the advective velocity, obtained in the continuum limit by

$$D(x_i) = \lim_{\substack{\Delta t \to 0 \\ \Delta x \to 0}} \frac{(\Delta x)^2}{2\Delta t}\left(q_i^{-1} + q_i^1\right), \tag{10}$$

$$v(x_i) = \lim_{\substack{\Delta t \to 0 \\ \Delta x \to 0}} \frac{\Delta x}{\Delta t}\left(q_i^1 - q_i^{-1}\right) - \frac{\partial}{\partial x} D(x_i). \tag{11}$$

Here we will assume homogeneous and unbiased jumps, such that $q_i^{-1} = q_i^1$ and $q_i^0 = 1 - q_i^{-1} - q_i^1$ are independent of i for all i. In this case, D is constant and $v = 0$. Dirichlet boundary conditions

$$n(b_\pm(t), t) = 0 \tag{12}$$

are imposed, which are equivalent to the absorbing boundary conditions described above for the discrete model by setting $q_{i_- -1}^1 = q_{i_+ +1}^{-1} = 0$.

2.2 Bone adaptation in response to osteocyte signals

In this section we describe our model for the adaptation of bone and of the osteocyte network in response to changes in mechanical loads. As shown schematically in Figure 1, we assume that the flux of signalling molecules at the boundaries of the network induces bone formation or bone resorption and corresponding evolutions of the bone boundaries.

According to our mechanotransduction model in Eqs (3) or (5), the production of signalling molecules is proportional to the mechanical simulus, and results in a certain flux of molecules at the boundary. Therefore, a high flux of signalling molecules emanating from the bone surface should induce bone formation, while a small flux of signalling molecules should induce bone resorption. We assume that there is a reference flux value J_0 at which the bone boundaries remain stationary. If the flux of signalling molecules at the bone surface exceeds J_0, then bone is overloaded and osteoblasts are generated to form bone. If the flux of signalling molecules is less than J_0, then bone is underloaded and osteoclasts are generated to resorb bone.

It is important to note here that J_0 is not a traditional mechanical setpoint, in the sense that it is not a local bone material property that can directly be compared with the local mechanical state of bone matrix (Lerebours & Buenzli 2016). The reference flux J_0 is associated with how osteoclasts and osteoblasts respond to mechanotransduced signals emanating from the bone surface, rather than with how osteocytes transduce local mechanical strains into biochemical signals. This distinction is absent in Wolff's-type laws in which there is a direct relationship between local mechanical stimuli and bone formation or bone resorption responses. Our model explicitly considers how local mechanical signals propagate through the network before inducing such bone responses.

Evolution of bone boundaries. The boundary positions in the discrete model are updated over a time step Δt based on the number of osteoblasts $\mathrm{Ob}_\pm(t)$ and osteoclasts $\mathrm{Oc}_\pm(t)$ at time t at the left boundary (indicated by $-$) and at the right boundary (indicated by $+$) according to:

$$\begin{aligned} b_-(t+\Delta t) &= b_-(t) - (k_\mathrm{f}\mathrm{Ob}_-(t) - k_\mathrm{r}\mathrm{Oc}_-(t))\Delta t, \\ b_+(t+\Delta t) &= b_+(t) + (k_\mathrm{f}\mathrm{Ob}_+(t) - k_\mathrm{r}\mathrm{Oc}_+(t))\Delta t, \end{aligned} \tag{13}$$

where $k_\mathrm{f} > 0$ and $k_\mathrm{r} > 0$ are the bone formation and bone resorption coefficients, respectively. These coefficients represent the length of bone produced or removed per cell per unit time, with units of μm/day. In the continuum limit as Δt approaches zero, Eqs (13) become

$$\frac{\mathrm{d}b_\pm}{\mathrm{d}t} = \pm(k_\mathrm{f}\mathrm{Ob}_\pm(t) - k_\mathrm{r}\mathrm{Oc}_\pm(t)). \tag{14}$$

Osteoblast and osteoclast generation. We consider two different models for the generation of osteoblasts and osteoclasts at the bone boundaries:

1. *Instantaneous cell generation model.* In this variant, the number of osteoblasts and osteoclasts at each bone boundary relates directly to the difference in flux of signalling molecules at the bone surface compared to the reference value J_0:

$$k_{\mathrm{f}}\mathrm{Ob}_{\pm}(t) = v_{\mathrm{f}}\left[\frac{J_{\pm}(t)-J_0}{J_0}\right]_+, \tag{15}$$

and

$$k_{\mathrm{r}}\mathrm{Oc}_{\pm}(t) = v_{\mathrm{r}}\left[\frac{J_0-J_{\pm}(t)}{J_0}\right]_+, \tag{16}$$

where $v_{\mathrm{f}} > 0$ and $v_{\mathrm{r}} > 0$ are bone formation and resorption speeds, respectively, with units of µm/day, and $[\cdot]_+$ indicates taking the positive part. This model reflects common Wolff's laws in which a bone apposition rate or bone resorption rate (in µm/day) is directly proportional to a mechanical stimulus, except that here this stimulus is a signal that propagates through the osteocyte network.

2. *Differential cell generation model.* In this model variant, it is the rate of change of the number of osteoblasts and osteoclasts at each bone boundary that relates to the difference in flux of signalling molecules at the bone surface compared to the reference value J_0:

$$\mathrm{Ob}_{\pm}(t+\Delta t) = \mathrm{Ob}_{\pm}(t) + \alpha_{\mathrm{Ob}}\left[\frac{J_{\pm}(t)-J_0}{J_0}\right]_+ \Delta t - A_{\mathrm{Ob}}\mathrm{Ob}_{\pm}(t)\Delta t, \tag{17}$$

and

$$\mathrm{Oc}_{\pm}(t+\Delta t) = \mathrm{Oc}_{\pm}(t) + \alpha_{\mathrm{Oc}}\left[\frac{J_0-J_{\pm}(t)}{J_0}\right]_+ \Delta t - A_{\mathrm{Oc}}\mathrm{Oc}_{\pm}(t)\Delta t, \tag{18}$$

respectively. The parameters α_{Ob}, α_{Oc} modulate the strength of osteoblast and osteoclast generation, and A_{Ob}, A_{Oc} specify the elimination rates of osteoblasts and osteoclasts. In the continuum limit $\Delta t \to 0$, Eqs (17) and (18) become differential equations for the population of osteoblasts and osteoclasts:

$$\frac{\mathrm{dOb}_{\pm}}{\mathrm{d}t} = \alpha_{\mathrm{Ob}}\left[\frac{J_{\pm}(t)-J_0}{J_0}\right]_+ - A_{\mathrm{Ob}}\mathrm{Ob}_{\pm}(t), \tag{19}$$

and

$$\frac{\mathrm{dOc}_{\pm}}{\mathrm{d}t} = \alpha_{\mathrm{Oc}}\left[\frac{J_0-J_{\pm}(t)}{J_0}\right]_+ - A_{\mathrm{Oc}}\mathrm{Oc}_{\pm}(t). \tag{20}$$

Osteocyte network evolution. When new bone is formed, we assume that a new osteocyte is created during a time increment Δt as soon as the bone surface extends a distance Δx from the osteocyte closest to the boundary (Fig. 1c). At the right boundary, this occurs when

$$b_+(t+\Delta t) \geqslant x_{i_+} + \Delta x \tag{21}$$

In this case, i_+ is incremented by one, i.e., $i_+(t+\Delta t) = i_+(t)+1$. The newly formed osteocyte is placed at $i_+(t+\Delta t)\Delta x$ and initiated with zero signalling molecules. It will start producing signalling molecules based on the reaction term $R_\sigma(x,t,N)$ in Eq. (3) or $R_\psi(x,t,N)$ in Eq. (5).

An osteocyte is removed from the network during a time increment Δt when bone resorption results in the bone surface moving past its position. At the right boundary, this occurs when

$$b_+(t+\Delta t) < x_{i_+} \tag{22}$$

Table 1 – List of all parameter values of the discrete model with differential cell generation.

Symbol	Value	Meaning
q_i^0	0.36	Fraction of signalling molecules that stay at the current osteocyte
q_i^{-1}, q_i^1	0.32	Fraction of signalling molecules that jump left and jump right
J_0	8.42262×10^7 /day	Threshold flux value
D	$3200000\,\mu\text{m}^2$/day	Diffusivity
Δt	10^{-5} day	Time step
W	$20\,\mu$m	Reference bone width of the cortical wall slice in the lateral direction
$\overline{L}$	$200\,\mu$m	Reference length of a mouse tibia cortical wall width
$\overline{F}$	0.04 N	Reference force exerting on a mouse tibia cross section
F_x	$5 \times 10^{-5}\,\text{N}/\mu\text{m}$	Force gradient in Section 3.4
$\overline{\sigma}$	10 MPa	Reference mechanical stress, related to $\overline{F}$, $\overline{L}$, and W by Eq. (7)
$\overline{\Psi}$	5×10^3 MPa	Reference strain energy density
λ_1	11059200/day	Creation rate of signalling molecules
λ_2	320/day	Degradation rate of signalling molecules
Λ_D	$100\,\mu$m	Diffusion length, related to D and λ_2 by Eq. (25)
$\rho = 1/\Delta x$	$0.1\,\mu\text{m}^{-1}$	Osteocyte density
α_{Ob}	0.04 /day	Creation rate of osteoblasts
α_{Oc}	0.2 /day	Creation rate of osteoclasts
A_{Ob}	0.2 /day	Elimination rate of osteoblasts
A_{Oc}	1 /day	Elimination rate of osteoclasts
k_{f}	$20\,\mu$m/day	Length of bone produced per cell per unit time
k_{r}	$100\,\mu$m/day	Length of bone removed per cell per unit time

In this case, i_+ is decremented by one, i.e., $i_+(t+\Delta t) = i_+(t) - 1$. Signalling molecules that were associated with the resorbed osteocyte are assumed to be freed into the microenvironment and to contribute to $N_+(t)$ used in Eqs (2) to calculate the flux of signalling molecules at the bone surface sensed by osteoblasts and osteoclasts (see Figure 1(d)). Similar considerations hold for the formation and removal of osteocytes at the left boundary.

Numerical simulations. To simulate our discrete model numerically, molecular occupancies and the fluxes of signalling molecules emanating from the bone surfaces are first evolved using Eqs (1)–(4). Populations of osteoblasts and osteoclasts are then calculated using either Eqs (15)–(16) (instantaneous cell generation model), or Eqs (17)–(18) (differential cell generation model). Finally, bone boundaries are evolved with Eqs (13) and the osteocyte network is updated based on Eqs (21)–(22). The discrete model is initialised with no osteoblasts nor osteoclasts, and molecular occupancies corresponding to the steady state of the continuum limit, see Section 2.3, Eq. (24). The model is then first evolved to steady state before perturbations in the loading force are applied. All parameter values of the model used in the numerical simulations are summarised in Table 1. Their estimation is detailed in Section 2.3.

2.3 Model calibration and parameter estimation

We now describe how we calibrate our mathematical model and select some of its parameters for biologically sensible behaviours.

We first consider the speed of transduced signal propagation through the osteocyte network

to estimate the jump paramaters q_i^0, q_i^{-1}, and q_i^1. In our previous work (Mehrpooya, Challis & Buenzli 2024), we presented an application of signal propagation in bone with an inhomogeneous density of osteocytes and second-neighbour jumps. Here, we restrict to nearest-neighbour jumps and homogeneous osteocyte density, and therefore adjust the jump probabilities slightly compared to this previous work. We set $q_i^0 = 0.36$, $q_i^{-1} = q_i^1 = 0.32$ over a time step of $\Delta t = 10^{-5}$ day for all i. In the continuum limit in Eqs (10)–(11), this corresponds to $D = 3.2\,\mathrm{mm}^2/\mathrm{day} \approx 37\,\mu\mathrm{m}^2/\mathrm{s}$ and $v = 0$. These values lead to reasonable rates of signal propagation through the osteocyte network, with a diffusive root mean square displacement of $\sqrt{2Dt} \approx 9\,\mu\mathrm{m}$ over one second, comparable to calcium signal travelling speeds of $2\,\mu\mathrm{m/s}$ (Turner & Forwood 1995) and fluid flow velocities of $20\,\mu\mathrm{m/s}$ (van Tol et al. 2020b).

The reaction rate parameters λ_1 and λ_2 influence the number of signalling molecules produced by osteocytes and emanating from the bone surface to induce bone formation or bone resorption. Some changes are required as well for values assumed for λ_1 and λ_2 compared to our previous work (Mehrpooya, Challis & Buenzli 2024), since we now include mechanics-dependent production rates to model osteocyte mechanotransduction in Eqs (3), (5). To ensure that bone adaptation to loading forces is consistent with experimental observations, we proceed in two steps. In a first step, we consider homeostatic steady states in which bone length L is adapted to a constant applied loading force F. These steady states provide a useful relationship $L(F)$ that enables us to estimate the reaction rate parameters λ_1, λ_2, and the threshold flux value J_0. In a second step, we consider the dynamics of bone adaptation leading to these homeostatic steady states, which enables us to estimate parameters influencing osteoblast and osteoclast populations.

Homeostatic steady states: bone length under constant loading force. To understand how λ_1, λ_2 and J_0 influence homeostatic steady states in which bone length is stationary under a constant loading force, we reason on the continuum model and determine the relationship $L(F)$ between an applied constant force F and the corresponding homeostatic bone length L. This kind of relationship is typical in Wolff's laws, in which the bone steady state is in a one-to-one relationship with the mechanical forces exerted on bone (Turner 1999; Lerebours & Buenzli 2016).

In steady state, $\partial n/\partial t = 0$ in Eq. (9) and $\mathrm{d}b_\pm/\mathrm{d}t = 0$ in Eq. (14). With the stress-dependent reaction rate from Eq. (3), Eq. (9) becomes

$$\frac{\mathrm{d}^2\overline{n}}{\mathrm{d}x^2} = -\frac{\lambda_1\rho}{D}\frac{\sigma}{\overline{\sigma}} + \frac{\lambda_2}{D}\overline{n}, \tag{23}$$

where $\overline{n}(x)$ is the steady-state concentration profile of signalling molecules within bone, and σ is constant and uniform due to the constant loading force, see Eq. (4). Equation (23) is an inhomogeneous second-order differential equation with constant coefficients. Since there is no bone boundary motion, we can always choose $b_\pm = \pm L/2$ for symmetry, where L is the fixed bone length. The solution to Eq. (23) with Dirichlet boundary conditions (Eq. (12)) at $x = \pm L/2$ is then given by

$$\overline{n}(x) = \rho\frac{\lambda_1}{\lambda_2}\frac{\sigma}{\overline{\sigma}}\left(1 - \frac{\cosh\left(\frac{x}{\Lambda_D}\right)}{\cosh\left(\frac{L}{2\Lambda_D}\right)}\right) \quad \text{for} \quad -\frac{L}{2} \leqslant x \leqslant \frac{L}{2}. \tag{24}$$

In Equation (24),

$$\Lambda_D = \sqrt{D/\lambda_2} \tag{25}$$

is the diffusion length of the signalling molecules, which represents the average distance that signalling molecules travel by diffusion during their lifetime $1/\lambda_2$. The parameter Λ_D controls the relative strength of diffusive transport over reaction. When Λ_D is large compared to the bone length L, transport dominates reaction and the continuum limit represents the discrete model well (Simpson et al. 2010; Li et al. 2022; VandenHeuvel, Buenzli & Simpson 2024; Mehrpooya, Challis & Buenzli 2024). The steady-state boundary fluxes $\overline{J}_\pm$ are given by

$$\overline{J}_\pm = \mp D \frac{\mathrm{d}\overline{n}}{\mathrm{d}x}(\pm L/2) = \rho\lambda_1\Lambda_D \frac{F/\overline{F}}{L/\overline{L}} \tanh\Big(\frac{L}{2\Lambda_D}\Big). \tag{26}$$

From Eq. (14), osteoblast and osteoclast populations in steady state, denoted by $\overline{\mathrm{Ob}}_\pm$ and $\overline{\mathrm{Oc}}_\pm$, respectively, are such that $k_\mathrm{f}\overline{\mathrm{Ob}}_\pm = k_\mathrm{r}\overline{\mathrm{Oc}}_\pm$. Therefore, the steady-state boundary fluxes $\overline{J}_\pm$ must satisfy

$$v_f \left[\frac{\overline{J}_\pm - J_0}{J_0}\right]_+ = v_r \left[\frac{J_0 - \overline{J}_\pm}{J_0}\right]_+ \tag{27}$$

with the instantaneous cell generation model (Eqs (15) and (16)), and

$$\frac{k_f \alpha_\mathrm{Ob}}{A_\mathrm{Ob}} \left[\frac{\overline{J}_\pm - J_0}{J_0}\right]_+ = \frac{k_r \alpha_\mathrm{Oc}}{A_\mathrm{Oc}} \left[\frac{J_0 - \overline{J}_\pm}{J_0}\right]_+ \tag{28}$$

with the instantaneous cell generation model (Eqs (19) and (20)). The only way to satisfy these equations is to have $\overline{J}_\pm = J_0$, which implies also that $\overline{\mathrm{Ob}}_\pm = \overline{\mathrm{Oc}}_\pm = 0$ in both models. Therefore, in steady state, the flux of signalling molecules emanating from the bone surface must equal the threshold value J_0, as expected, so that with Eq. (26),

$$J_0 = \rho\lambda_1\Lambda_D \frac{F/\overline{F}}{L/\overline{L}} \tanh\Big(\frac{L}{2\Lambda_D}\Big). \tag{29}$$

We can recast Eq. (29) to obtain an explicit relationship $F(L)$ between the applied loading force F and the homeostatic bone length L, which depends on the choice of several parameters:

$$F(L) = \frac{J_0\overline{F}}{\rho\lambda_1\overline{L}} \frac{L/\Lambda_D}{\tanh\Big(\frac{L}{2\Lambda_D}\Big)}. \tag{30}$$

Inverting this equation determines an effective steady-state Wolff's law $L(F)$. Figure 2 shows the curve $F(L)$ plotted for different values of Λ_D when all curves go through the point $(\overline{L}, \overline{F})$, which occurs when the parameters satisfy

$$\frac{J_0}{\rho\lambda_1} = \Lambda_D \tanh\Big(\frac{\overline{L}}{2\Lambda_D}\Big). \tag{31}$$

In this case, Eq. (30) can be recast as

$$F(L) = \overline{F}\,\frac{L}{\overline{L}}\,\frac{\tanh\Big(\frac{\overline{L}}{2\Lambda_D}\Big)}{\tanh\Big(\frac{L}{2\Lambda_D}\Big)}. \tag{32}$$

In this expression for $F(L)$, the diffusion length Λ_D affects both the steepness of $F(L)$ for $L \gg \Lambda_D$, and the width of the region $0 \leqslant L \lesssim \Lambda_D$ in which $F(L)$ does not vary significantly (Figure 2). Given our choice of reference mouse tibia cortical wall width $\overline{L} = 200\,\mu\mathrm{m}$, we set $\Lambda_D = 100\,\mu\mathrm{m}$.

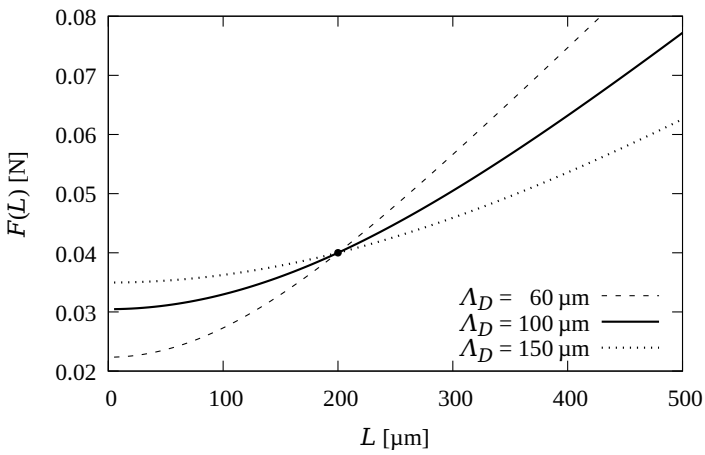

Figure 2 – Relationship between loading force F and homeostatic bone length L with $\overline{L} = 200\,\mu\text{m}$ and $\overline{F} = 0.04\,\text{N}$ in Eq. (32) for $\Lambda_D = 60\,\mu\text{m}$, $100\,\mu\text{m}$, and $150\,\mu\text{m}$.

This value of Λ_D is large enough for diffusion-dominated signal propagation so the continuum limit matches the discrete model, yet small enough so that small changes in F do not cause excessive changes in L.

Having set $D = 3.2 \times 10^6\,\mu\text{m}^2/\text{day}$ and $\Lambda_D = 100\,\mu\text{m}$, the degradation rate of signalling molecules is determined from Eq. (25) to be $\lambda_2 = 320/\text{day}$. From Eq. (31) with $\rho = 1/\Delta x = 0.1\,\mu\text{m}^{-1}$, we must also have $J_0/\lambda_1 = 10\tanh(1) \approx 7.62$, and so we finally set $\lambda_1 = 128/\text{s} = 11{,}059{,}200/\text{day}$, and $J_0 = 84226220/\text{day}$. The value of λ_1 scales the number of signalling molecules at osteocytes in steady state. Here it is chosen to be slightly larger than values used in our previous work (Mehrpooya, Challis & Buenzli 2024).

As illustrated above, the continuum limit of the discrete model is particularly useful to reason qualitatively and quantitatively on the behaviour of the discrete model. We have used these behaviours to determine key parameter values associated with signal propagation and steady-state configurations so they are consistent with expected bone adaptation properties. To ensure that these properties carry over to the discrete model, we assess in Figure 3 the discrepancy between the discrete model and its continuum limit in steady state using the parameters estimated so far. We compare the steady state of the discrete model for a fixed bone length of $200\,\mu\text{m}$ and a uniform loading force $\overline{F} = 0.04\,\text{N}$ with the continuum steady state $\overline{n}(x)$ from Eq. (24). Figure 3 shows that there is a good match between the steady state molecule concentration profiles of the discrete and continuum models (gray histogram bars and dashed red curved, respectively), and a good match between the continuum and discrete boundary fluxes (black and red slopes). The flux discrepancy between the discrete and continuum models is about 7.5%.

Osteoblast and osteoclast parameters. The remaining parameters of the model, k_f, k_r, and either υ_f and υ_r (instantaneous cell generation model) or α_Ob, α_Oc, A_Ob, A_Oc (differential cell generation model) are associated with the population of osteoblasts and osteoclasts. These parameters are estimated in Appendix A based on the dynamics of bone adaptation to steady state under a 20% increase in the force. In brief, the instantaneous cell generation model with moving boundaries leads to biologically unrealistic instabilities in the form of oscillations of increasing amplitude in the flux of signalling molecules and in boundary positions (Section A.1). These oscillations are not overcome by tuning υ_f and υ_r. We therefore do not consider the instantaneous cell generation model further, except in the analysis of bone behaviour under a force gradient in Section 3.4. The instabilities of the instantaneous cell generation model are

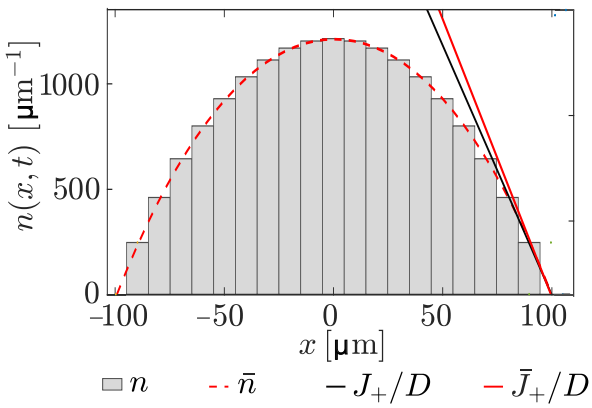

Figure 3 – Comparison of the steady state calculated from the discrete and continuum models with fixed boundaries and uniform loading force. Molecule concentrations corresponding to the discrete (grey) and exact (red dashed) solutions at steady state for a bone length of 200 μm. The solid black line represents the slope $\partial n/\partial x = -J_+/D$ of the discrete concentration at the right boundary, calculated as $n_{i+}/\Delta x$. The solid red line represents the slope of the continuum concentration at the right boundary, calculated as $\partial \overline{n}/\partial x(L/2)$ from Eq. (24).

resolved by the differential cell generation model, which takes into account the fact that the generation of osteoblasts and osteoclasts in response to mechanical signals takes some time. While oscillations in boundary positions may still occur for some parameter combinations in the differential cell generation model, these oscillations are stable, and a parameter regime can be devised in which these oscillations are overdamped (Section A.2).

3 Results and discussion

In this section we first determine steady states of the discrete model reached by initialising it with steady states of the continuum model for a variety of bone lengths L and loading forces F. We then present a range of numerical results that demonstrate key features of our discrete model for bone mechanical adaptation under temporal and spatial variations of the loading force.

Figure 4 highlights the difference in steady-state lengths obtained for constant loading forces in the continuum model (red curve, given by Eq. (30)) and in the discrete model (grey dots). The discrete simulations are initialised from the continuum steady states by setting signalling molecule occupancies as $N_i(0) = \Delta x\, \overline{n}(x_i)$, where $\overline{n}(x)$ is the steady-state concentration of the continuum model in Eq. (24), and by setting initial lengths $L(0)$ by inverting $F(L)$ in Eq. (30). The time evolution of the discrete model is illustrated in this figure by trajectories $\big(L(t), F\big)$ (grey lines) ending at the discrete model steady state (grey dots). Overall there is a good match between the steady-state lengths obtained with the discrete and continuum models. However, at all values of the applied loading force, the equilibrium states of the discrete model have a slightly shorter bone length compared to the equilibrium states predicted by the continuous model. The match improves at lower values of L, as expected based on the continuum limit being valid for $\Lambda_D \gg L$ (VandenHeuvel, Buenzli & Simpson 2024; Mehrpooya, Challis & Buenzli 2024). In our subsequent numerical simulations, we initialise the discrete model with the steady states obtained from the continuum model, but always wait until the discrete model reaches a steady state before varying the loading force.

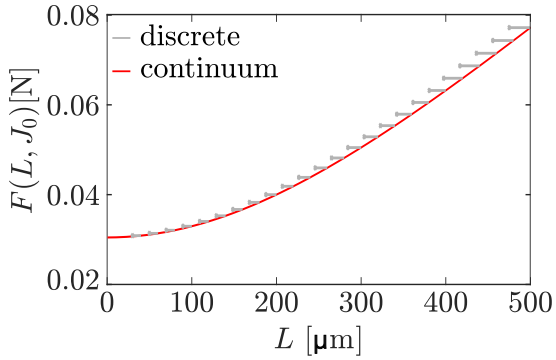

Figure 4 – Discrete model trajectories of the bone length (grey lines) alongside the continuum steady-state bone length (red curve) for different uniform loading forces and initial network lengths.

3.1 Bone response to overloading followed by unloading

We now examine the response of the discrete model under a cycle of overloading and unloading. We assume that the steady-state force $F = \overline{F}$ is first uniformly increased by 20% at $t = 40$ day, from $F = 0.04$ N to $F = 0.048$ N, and then restored to its initial value $F = 0.04$ N at $t = 200$ days.

Snapshots of the concentration profiles $n(x_i, t)$ at each osteocyte location at various times are shown in Figure 5 (grey bars) and compared with the steady-state concentration profiles $\overline{n}(x)$ from Eq. (24), where L is taken as $L = b_+(t) - b_-(t)$ (red dashed line). There is a good match between the discrete model concentrations and the continuum profiles, despite the continuum profiles assuming a steady state, indicating that the dynamics of molecular signalling is fast compared to the dynamics of bone changes.

Figure 6a illustrates the time evolution of the relationship between bone length and mechanical force by plotting the trajectory $\big(L(t), F(t)\big)$ (blue). This trajectory begins at $(\overline{L}, \overline{F})$ on the $F(L)$ curve given by Eq. (30) (red). It first evolves to $(L_{\text{final}}, \overline{F})$, where L_{final} denotes the steady-state bone length in the discrete model for the force $\overline{F}$. After the force is increased at $t = 40$ days, bone length increases and the trajectory tends toward the $F(L)$ curve with a higher value of F. After restoring the force to its initial value $\overline{F}$ at $t = 200$ days, bone length returns to its steady-state bone length L_{final}.

The evolution of the population of osteoclasts and osteoblasts and of the flux of signalling molecules emanating from the bone surfaces during the overloading and unloading cycle are shown in Figures 6c and 6d, respectively. The population of osteoclasts at early times $t < 40$ day is generated due to the flux $J_\pm$ being initially slightly lower than the reference value J_0. This difference is due to J_0 being estimated from the steady state of the continuum limit while $J_\pm$ are calculated from the discrete model (see Section 2.3 and Figure 3). This initial bone resorption explains why the steady-state length of the discrete model is slightly less than that predicted from the continuum model by the $F(L)$ curve.

The force increase at $t = 40$ day first leads to an increase in the production of signalling molecules within the osteocyte network. This surplus of signalling molecules propagates to the bone surface and induces an increase in boundary fluxes $J_\pm$, which in turn stimulates osteoblast generation (Figure 6c) and bone growth (Figure 6b). The formation of osteocytes in this overloading phase is marked by steps in the evolutions of $i_\pm(t)\Delta x$ in Figure 6b. When a new osteocyte is formed at the growing bone boundary, it has no signalling molecules. This induces a sudden, but short-lived decrease in the boundary fluxes (Figure 6d), until the new osteocyte

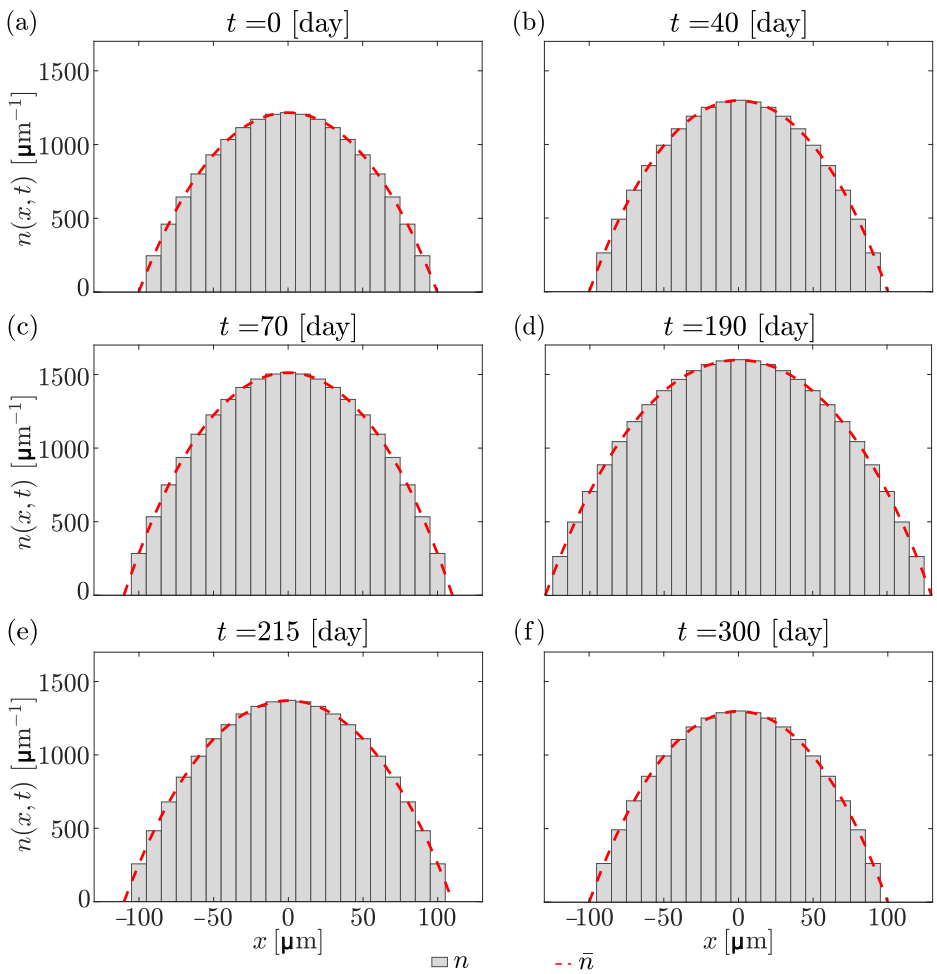

Figure 5 – Snapshots of concentration profiles $n(x_i, t)$ (grey bars) and steady-state concentration profiles $\overline{n}(x)$ from Eq. (24) shown at various times. (a) Initial condition $t = 0$; (b) Steady state of the discrete model, $t = 40$ days; (c) Intermediate state during the formation phase, $t = 70$ days; (d) New steady state reached after the force increase, $t = 190$ days; (e) Intermediate state during the resorption phase, $t = 215$ days; (f) Final steady state after return to the initial loading force, matching the state at $t = 40$ days.

collects signalling molecules from its neighbour and from its own production. Bone length continues to increase until the boundary fluxes $J_\pm$ converge toward the reference value J_0.

Interestingly, during this formation phase, the pointwise generation of osteocytes and its effect on boundary fluxes disrupts the population of osteoblasts, which exhibits several small peaks (Figure 6c). It is possible that these kinds of discrete behaviours could be related to the formation of regular spatial patterns seen in lamellar bone, in which bone is produced in distinct layers called lamellae, with possibly layered osteocyte generation (Martin, Burr & Sharkey 1998; Marotti 1992; Ardizzoni 2001).

When the force is restored at $t = 200$ day, osteocytes within the network decrease their production of signalling molecules. This depletion of signalling molecules propagates to the bone surface where it induces a reduction in boundary fluxes $J_\pm$, which in turn stimulates osteoclast generation (Figure 6c) and leads to bone loss (Figure 6b). Osteocyte resorption is marked by steps in the evolutions of $i_\pm(t)\Delta x$. When an osteocyte is resorbed, its signalling molecules are freed into the micro-environment. This generates a strong, but short-lived spike in the boundary fluxes (Figure 6d). The steady steady state is reached when the boundary fluxes reach the reference value J_0.

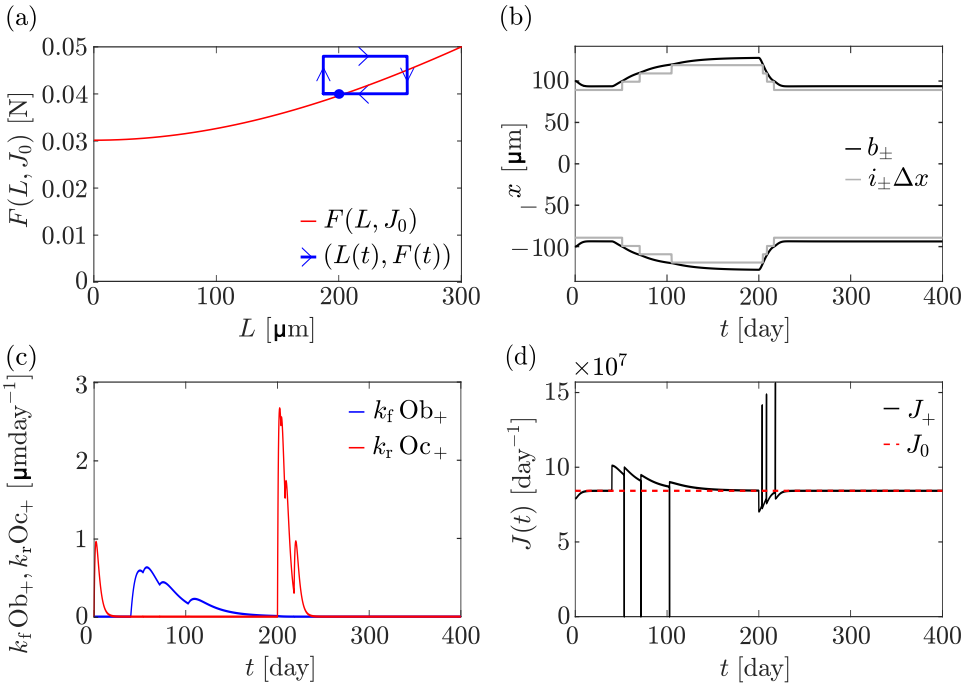

Figure 6 – Overloading the differential cell generation model with a 20% force increase from $F = 0.04\,\mathrm{N}$ to $F = 0.048\,\mathrm{N}$ at $t = 40\,\mathrm{day}$, followed by a return to $F = 0.04\,\mathrm{N}$ at $t = 200\,\mathrm{day}$. (a) The relationship between network length and mechanical force derived from the continuum model (red line), and the trajectory of the network length over the discrete model simulation (blue line). The blue dot represents both $(\overline{L}, \overline{F})$ and $(L_{\mathrm{final}}, \overline{F})$, which coincide. (b) Evolution of $i_\pm \Delta x$ (grey lines), along with the left and right boundary positions (black lines) over time. (c) Speed of osteoblast-driven (blue line) and osteoclast-driven (red line) boundary movement at the right boundary over time. (d) Evolution of the flux at the right boundary for the discrete model (black line), with the reference value J_0 shown (red dashed line).

3.2 Bone response to unloading followed by reloading

We now examine the model's behaviour when unloading occurs before reloading. We assume that the steady-state force $F = \overline{F}$ is first uniformly reduced by 20% at $t = 40\,\mathrm{day}$, i.e., from $F = 0.04\,\mathrm{N}$ to $F = 0.032\,\mathrm{N}$, and then restored to its initial value $F = 0.04\,\mathrm{N}$ at $t = 200\,\mathrm{day}$.

The trajectory $\big(L(t), F(t)\big)$ in Figure 7a (blue) shows a similar pattern as in Figure 6a, where there is first a period of bone length relaxation to the steady state of the discrete model. When the force is reduced at $t = 40\,\mathrm{days}$, bone length decreases and the trajectory tends toward the $F(L)$ curve at the reduced value of F. After restoring the force to its initial value $\overline{F}$ at $t = 200\,\mathrm{days}$, bone length increases and converges to a value L_{final}. However, here, the final bone length does not converge back to the initial steady-state length of the discrete model. The trajectory is not closed, meaning that bone length is not fully recovered after the force is restored to its initial value. This is also visible from the evolution of boundary positions $b_\pm(t)$ in Figure 7b.

Figure 7b shows that while four osteocytes are resorbed at either ends during the unloading phase, only three are re-generated during the reloading phase. This behaviour shows that history dependence of the bone state may arise due to the discrete nature of osteocytes accounted for in our discrete model. Such history dependence is not possible in the continuum model, where steady-state lengths under a constant uniform force are always unique, and characterised by the curve $F(L)$.

The evolution of the population of osteoclasts and osteoblasts and of the boundary fluxes of

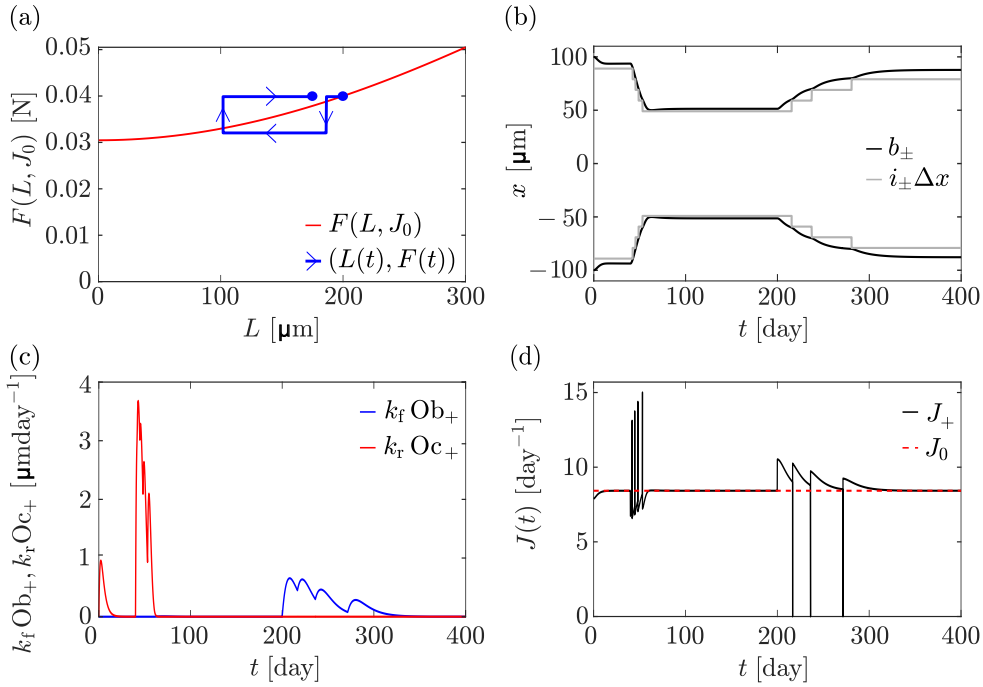

Figure 7 – Underloading the differential cell generation model with a 20 % force reduction from $F = 0.04\,\mathrm{N}$ to $F = 0.032\,\mathrm{N}$ at $t = 40\,\mathrm{day}$, followed by a return to $F = 0.04\,\mathrm{N}$ at $t = 200\,\mathrm{day}$. (a) The relationship between network length and mechanical force derived from the continuum model (red line), and the trajectory of the network length over the discrete model simulation (blue line). The blue dots illustrate $(\overline{L}, \overline{F})$ and $(L_{\mathrm{final}}, \overline{F})$, where L_{final} represents the final network length when the system reaches a steady state. (b) Evolution of $i_\pm \Delta x$ (grey lines), along with the left and right boundary positions (black lines) over time. (c) Speed of osteoblast-driven (blue line) and osteoclast-driven (red line) boundary movement at the right boundary over time. (d) Evolution of the flux at the right boundary for the discrete model (black line), with the reference value J_0 shown (red dashed line). Parameters: $J_0 = 8.42262 \times 10^7\,/\mathrm{day}$, $D = 3200000\,\mu\mathrm{m}^2/\mathrm{day}$, $\Delta t = 10^{-5}\,\mathrm{day}$, $K = 21$, $\overline{L} = 200\,\mu\mathrm{m}$, $\overline{F} = 0.04\,\mathrm{N}$, $F = 0.04\,\mathrm{N}$, $\lambda_1 = 11059200/\mathrm{day}$, $\lambda_2 = 320/\mathrm{day}$, $\alpha_{\mathrm{Ob}} = 0.04\,/\mathrm{day}$, $\alpha_{\mathrm{Oc}} = 0.2\,/\mathrm{day}$, $A_{\mathrm{Ob}} = 0.2\,/\mathrm{day}$, $A_{\mathrm{Oc}} = 1\,/\mathrm{day}$, $k_f = 20\,\mathrm{day}$, and $k_r = 100\,\mathrm{day}$.

signalling molecules exhibit similar qualitative patterns as in Figure 6. The temporary increases in osteoblasts after each osteocyte generation are more pronounced than in Figure 6. This may be due to bone possessing a lower number of osteocytes, and therefore being more strongly affected by an osteocyte formation. The fact that bone length is not fully restored after the force is returned to its initial value may also be an effect of small osteocyte numbers.

3.3 Disuse

The force–length relationship $F(L)$ in Eq. (30) shows that the steady-state bone length goes to zero for a loading force $F(0) \approx 0.0304\,\mathrm{N}$ (Figure 2). This suggests that $F(0)$ is a threshold force below which all bone is resorbed. In Figure 8, we simulate a disuse situation in which the loading force is reduced below the threshold to $F = 0.02\,\mathrm{N}$ at $t = 20\,\mathrm{days}$. Contrary to the 20% unloading situation of Figure 7, here the bone is fully resorbed. The initial decrease in boundary fluxes at the onset of disuse generates osteoclasts that decrease bone length. Mechanical stresses in Eq. (4) increase with time due to the loss of bone, which stimulates signalling molecule production to compensate their initial depletion. However, these signalling molecules are produced by a

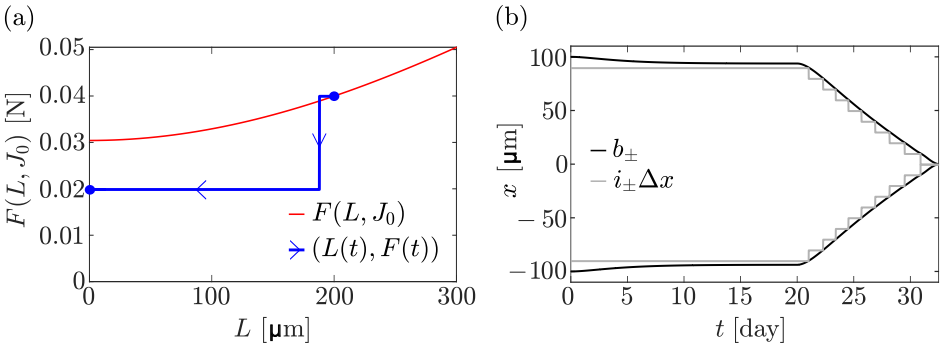

Figure 8 – Unloading the differential cell generation model with a force reduction to $F = 0.02\,\mathrm{N}$ at $t = 20\,\mathrm{days}$, which is below the predicted minimum mechanical force threshold. (a) The relationship between network length and mechanical force predicted by the continuum model (red line), and the trajectory of the network length over the discrete model simulation (blue line). The blue dots illustrate $(\overline{L}, \overline{F})$ and $(0, 0.02)$. (b) Evolution of $i_\pm \Delta x$ (grey lines), along with the left and right boundary positions (black lines) over time.

decreasing number of osteocytes and the boundary fluxes of signalling molecules remain below the reference value J_0 at all times until all the bone is resorbed.

The destructive competition between the increase in signalling molecule production and the loss of osteocytes in this disuse situation can be overcome if a different mechanotransduction model is chosen, so that molecule production increases faster as bone is lost. This occurs for example if we assume that osteocytes produce signalling molecules in response to strain energy density $\Psi(x, t)$ in Eqs (5)–(6). In this case, the relationship in Eq. (29) between the reference flux J_0, the loading force F, and the bone length L in homeostatic steady states becomes

$$J_0 = \rho \lambda_1 \Lambda_D \frac{(F/L)^2}{(\overline{F}/\overline{L})^2} \tanh\left(\frac{L}{2\Lambda_D}\right). \tag{33}$$

The relationship between loading force and homeostatic bone length found from Eq. (33) changes to

$$F(L) = \overline{F}\,\frac{L}{\overline{L}} \sqrt{\frac{\tanh\left(\frac{\overline{L}}{2\Lambda_D}\right)}{\tanh\left(\frac{L}{2\Lambda_D}\right)}}, \tag{34}$$

where parameters are chosen as in Eq. (31) so that $\overline{F} = F\left(\overline{L}\right)$. For small bone lengths, Eq. (34) shows that $F(L) \propto \sqrt{L}$, or, equivalently, $L(F) \propto F^2$. This relationship is more protective of bone loss for small forces, and total bone loss is only obtained when $F = 0$. This is illustrated in Figure 9, in which the same disuse situation as in Figure 8 is simulated, but with a strain energy density stimulation of signalling molecule production by osteocytes (Eqs (5)–(6)). In this case, the production of signalling molecules increases quadratically with $1/L$ as bone length reduces. This increase in production rate is strong enough to compensate for the loss of osteocytes, and bone length reaches a nonzero steady state (Figure 9b).

The difference in behaviour of our model when osteocyte mechanotransduction is based on mechanical stress or when it is based on strain energy density is significant in a disuse situation. Wolff's laws and similar mechanostat models predict that disuse leads to full resorption of bone, but this is only predicted for a zero loading force (Turner 1999; Skerry 2008). Our model show that accounting for signal propagation through the osteocyte network enables new behaviours.

Disuse due to prolonged bedrest, spinal cord injury, and spaceflight missions shows that bone loss slows down and does not lead to complete loss. However, protective mechanisms

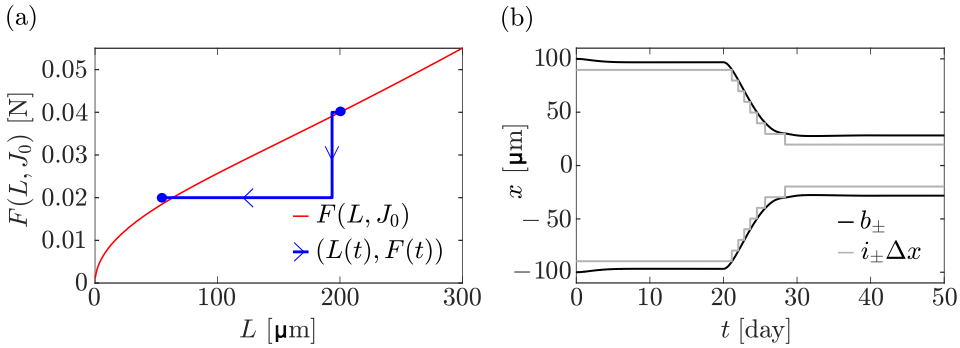

Figure 9 – Unloading the differential cell generation model with SED stimulation by reducing the force to $F = 0.02\,\mathrm{N}$ at $t = 20\,\mathrm{day}$. (a) The relationship $F(L)$ between bone length and loading force predicted by the continuum model for SED stimulation in Eq. (34) is shown as the red line, and the trajectory $\big(L(t), F(t)\big)$ is shown as the blue line. The blue dots mark $(\overline{L}, \overline{F})$ and $(L_{\text{final}}, 0.02)$, where L_{final} represents the final network length when the system reaches a steady state. (b) Evolution of $i_\pm \Delta x$ (grey lines), along with the left and right boundary positions (black lines) over time.

such as osteocyte accommodation are thought to be at play in these situations (Turner 1999; Lerebours & Buenzli 2016). Our model does not account for such mechanisms. The existence of a threshold loading force below which all bone is resorbed in our model may not represent bone behaviour at a macroscopic scale. However, it could represent a tipping mechanism at a small scale during the structural optimisation of trabecular bone, by which trabecular struts are entirely resorbed as soon as the load they carry falls below a threshold.

3.4 Mechanical adaptation to a force gradient

We now investigate how our model predicts the mechanical adaptation of bone under a inhomogenous loading force

$$F(x) = \overline{F} + F_x x. \tag{35}$$

This force field can be thought of as that generated under compression (baseline $\overline{F}$) and bending (gradient F_x) over one side of the cortical wall (Figure 1). For this simulation, we use the stress-induced mechanostransduction model (Eqs (3)–(4)) and suppose that bone initially occupies the domain $-200\,\mu\mathrm{m} \leqslant x \leqslant 0$. We choose a gradient value $F_x = 5\times10^{-5}\,\mathrm{N}/\mu\mathrm{m}$ so that $F(-200\,\mu\mathrm{m}) = 0.03\,\mathrm{N}$, which is marginally under the homogeneous loading force threshold $0.0304\,\mathrm{N}$ below which bone is fully resorbed (see Section 3.3).

Figure 10 shows that under this force gradient, bone is first resorbed quickly at the left boundary until that boundary has moved into a region where the force value is above the full-resorption threshold. At the same time, bone is formed at the right boundary. The bone drifts in space toward greater values of x, with increasing speed (Figure 10c). The speed at the right boundary is also greater than the speed at the left boundary, which results in an approximately linearly increasing bone length at large times (Figure 10d). The sequential removal of osteocytes at the left boundary and formation of new osteocytes at the right boundary leads to regular spikes in the boundary fluxes (Figure 10b), which generate sizeable fluctuations in the osteoclast and osteoblast populations (Figure 10e,f).

The simulations in Figure 10 suggest that bone does not reach a steady state. The increasing force value with x seen by the moving right boundary always induces more bone formation.

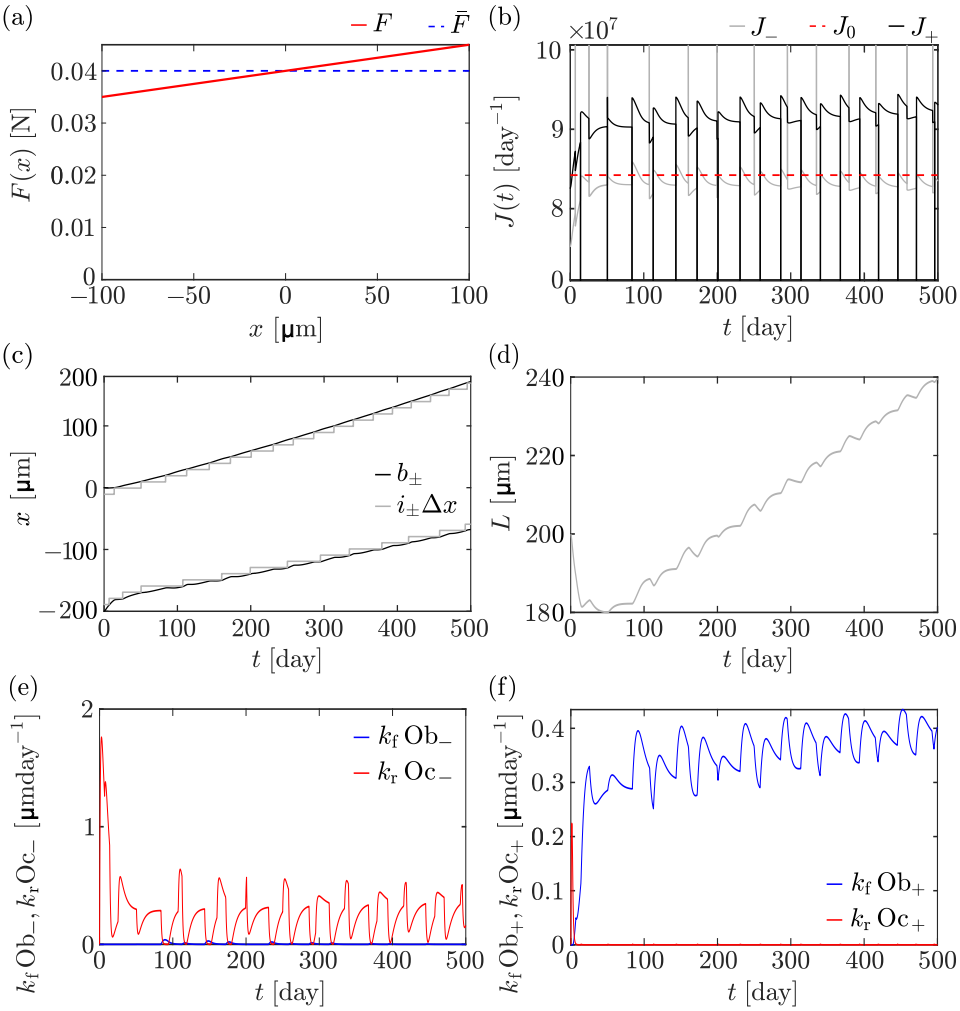

Figure 10 – Differential cell generation model with stress stimulation and a force gradient. (a) The applied gradient force (red line), with the reference force $\overline{F} = 0.04\,\mathrm{N}$ shown (blue dashed line). (b) Evolution of the discrete model flux at the left boundary (grey line) and the right boundary (black line), with the reference value J_0 shown (red dashed line). (c) Evolution of $i_\pm \Delta x$ (grey lines), along with the left and right boundary positions (black lines). (d) Evolution of network length over time. (e–f) Speed of osteoblast-driven (blue line) and osteoclast-driven (red line) boundary movement at the left boundary (e) and right boundary (f) over time.

This is a known shortcoming of commonly used Wolff's laws and mechanostats, that requires other mechanisms such as osteocyte desensitisation or osteocyte network adaptation to be resolved (Levenston et al. 1998; Turner 1999; Lerebours & Buenzli 2016; Lerebours 2017).

The evolution of the bone boundaries occurs over long timescales, which suggests that the concentration profile of signalling molecules in the network is in a quasi-steady state that evolves slowly due to bone boundary movement. The homeostatic relationship $F(L)$ in Eq. (30) no longer holds since the force is now inhomogenous, but some insights into the adaptation of bone under a force gradient in our model can be inferred by assuming a quasi-steady state $\partial n/\partial t = 0$ with the force $F(x)$ given in Eq. (35). In quasi-steady state, the concentration profile $n(x)$ of signalling molecules is solution of Eq. (23) with

$$\frac{\sigma(x)}{\overline{\sigma}} = \frac{\overline{F} + F_x x}{(b_+ - b_-)W}, \tag{36}$$

where b_+ and b_- are assumed to evolve slowly enough to be approximately constant. With the

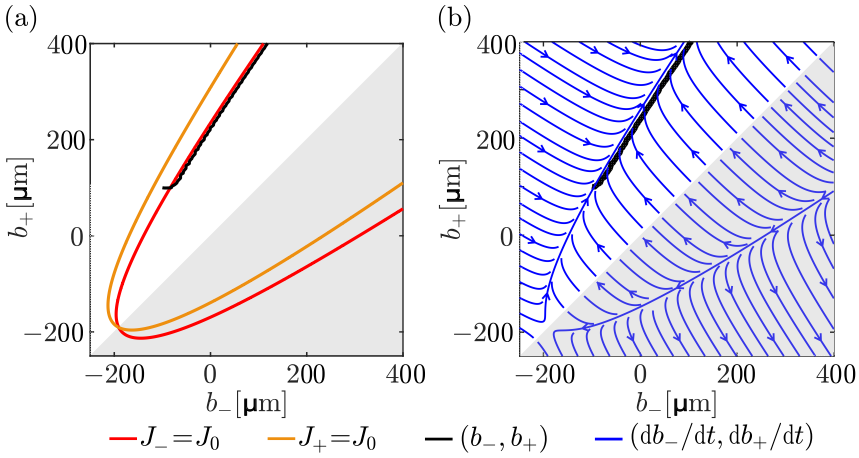

Figure 11 – (a) Contour plots of $J_- = J_0$ (red) and $J_+ = J_0$ (blue) for the continuum differential cell generation model in the (b_-, b_+)-plane, along with the trajectory of $(b_-(t), b_+(t))$ (black) corresponding to the simulation in Figure 10. (b) Phase portrait of $\left(\frac{db_-}{dt}, \frac{db_+}{dt}\right)$ for the instantaneous cell generation model with $v_f = v_r = v_0 = 10\,\mu\text{m/day}$ (blue) and the (b_-, b_+) trajectory (black) corresponding to the simulation in Figure 10. The grey shaded area represents a non-physical region. Both figures highlight the dynamics of the boundaries under the influence of mechanical stimuli, with the contour and phase plots illustrating the system's evolution over time. Parameters are the same as Figure 10.

boundary conditions

$$n(b_-) = 0, \qquad n(b_+) = 0, \tag{37}$$

the quasi-state solution is given by

$$n(x) = \rho \frac{\lambda_1}{\lambda_2} \left(\frac{\sigma(x)}{\overline{\sigma}} - \frac{\sigma(b_+)}{\overline{\sigma}} \frac{\sinh\left(\frac{x-b_-}{\Lambda_D}\right)}{\sinh\left(\frac{b_+-b_-}{\Lambda_D}\right)} - \frac{\sigma(b_-)}{\overline{\sigma}} \frac{\sinh\left(\frac{b_+-x}{\Lambda_D}\right)}{\sinh\left(\frac{b_+-b_-}{\Lambda_D}\right)} \right). \tag{38}$$

When $b_- = -L/2$, $b_+ = L/2$ and $F_x = 0$, Eq. (38) falls back onto Eq. (24). The boundary fluxes $J_\pm = \mp D\,dn/dx(b_\pm)$ are now functions of both b_- and b_+ independently, rather than being functions of only the combination $L = b_+ - b_-$, as was the case for a homogeneous loading force:

$$J_-(b_-, b_+) = D\rho \frac{\lambda_1}{\lambda_2} \left(\frac{F_x}{\overline{F}} \frac{\overline{L}}{b_+ - b_-} - \frac{\sigma(b_+)}{\Lambda_D \overline{\sigma}} \frac{1}{\sinh\left(\frac{b_+-b_-}{\Lambda_D}\right)} + \frac{\sigma(b_-)}{\Lambda_D \overline{\sigma}} \coth\left(\frac{b_+ - b_-}{\Lambda_D}\right) \right), \tag{39}$$

$$J_+(b_-, b_+) = -D\rho \frac{\lambda_1}{\lambda_2} \left(\frac{F_x}{\overline{F}} \frac{\overline{L}}{b_+ - b_-} - \frac{\sigma(b_+)}{\Lambda_D \overline{\sigma}} \coth\left(\frac{b_+ - b_-}{\Lambda_D}\right) + \frac{\sigma(b_-)}{\Lambda_D \overline{\sigma}} \frac{1}{\sinh\left(\frac{b_+-b_-}{\Lambda_D}\right)} \right). \tag{40}$$

In Figure 11a, we plot the isoflux contour lines $J_-(b_-, b_+) = J_0$ and $J_+(b_-, b_+) = J_0$ in (b_-, b_+) space. A homeostatic steady state is characterised by both boundary fluxes matching the reference value J_0 (see Section 2.3), which is at the intersection of these isoflux contours. The only steady state occurs when $b_- = b_+$, i.e., for zero bone length, and at a specific location in space where the force value corresponds to the full-resorption threshold, i.e., where $F(b_-) = 0.0304\,\text{N}$. Indeed, one can show from Eqs (39)–(40) that

$$\lim_{b_+ \to b_-} J_\pm(b_-, b_+) = \frac{\rho \lambda_1 \overline{L}}{2\overline{F}} (\overline{F} + F_x b_-), \tag{41}$$

so that when $J_+(b_-, b_-) = J_-(b_-, b_-) = J_0$ with $J_0 = \rho\lambda_1\Lambda_D \tanh\big(\overline{L}/(2\Lambda_D)\big)$ (see Eq. (31)), b_- is such that

$$\overline{F} + F_x b_- = 2\Lambda_D \frac{\overline{F}}{\overline{L}} \tanh\left(\frac{\overline{L}}{2\Lambda_D}\right). \tag{42}$$

The right hand side in Eq. (42) corresponds to the full-resorption threshold obtained as $\lim_{L\to 0} F(L)$ in Eq. (32). Solving Eq. (42) for b_- gives the only homeostatic steady state $b_- = b_+ \approx -190.7\,\mu\text{m}$.

Figure 11a also depicts the trajectory $\big(b_-(t), b_+(t)\big)$ followed by the numerical simulations of the discrete model (black line). This trajectory closely follows the $J_-(b_-, b_+) = J_0$ isoflux line, which means that the flux at the left boundary is close to the reference value at all times, as seen also in Figure 10b. However, the position of the left boundary cannot remain stationary. The right boundary flux is always greater than J_0 on average (Figures 10b and 11a). The increase of b_+ due to bone formation at the right boundary forces b_- to increase as well by following the curve $J_-(b_-, b_+) = J_0$.

A phase portrait of the evolution of the bone boundaries under the quasi-state approximation can be obtained in the continuum limit of the instantaneous cell generation model when $v_f = v_r = v$. In this case, the evolution equations (14)–(16) become

$$\frac{\mathrm{d}b_-}{\mathrm{d}t} = v\frac{J_-(b_-, b_+) - J_0}{J_0}, \tag{43}$$

$$\frac{\mathrm{d}b_+}{\mathrm{d}t} = v\frac{J_+(b_-, b_+) - J_0}{J_0}, \tag{44}$$

where $J_\pm(b_-, b_+)$ are given by Eqs (39)–(40). Figure 11b shows that the trajectory $\big(b_-(t), b_+(t)\big)$ followed by the discrete simulation with the differential cell generation model follows the field lines of the continuum dynamical system of Eqs (43)–(44) very well. The phase portrait in Figure 11b shows that bone will continue to increase the position of both boundaries while also increasing its length. These results show that while the instantaneous cell generation model leads to instabilities in simulations of the discrete model, its continuum limit may still prove useful in analysing phase portraits of the evolution of bone. Such analyses may provide good indications of how further mechanisms may ensure that bone does not grow unbounded under compression and bending.

4 Conclusion

This paper presents a novel mathematical model of bone adaptation that takes into account explicitly the propagation of signalling molecules in the osteocyte network as a signalling mechanism to induce bone formation or bone resorption. The model is based on a simple one-dimensional osteocyte network, where molecules are generated by osteocytes in response to mechanical stimulus, and where these molecules jump from one osteocyte to the next until they reach the bone surface. The explicit inclusion of signal propagation through a dynamic network of osteocytes in this model leads to new behaviours compared to previous continuum models of bone adaptation. Cycles of unloading and reloading may not always restore bone to its initial state. Furthermore, when osteocytes are stimulated by mechanical stress, our model predicts the emergence of a minimum threshold of loading force below which all bone is resorbed. However, no such minimum threshold is predicted when osteocytes are stimulated by the strain energy density. These kinds of qualitatively distinct behaviours may be useful in determining what

mechanical cues osteocytes are most sensitive to in responding to mechanical stimulus. These cues still remains largely unknown, particularly for networks composed of few osteocytes, such as in trabecular struts.

The consideration of osteocyte creation during bone formation and osteocyte removal during bone resorption leads to regular disruptions in signalling molecules emanating from the bone surface, which in turn leads to periodic variations in the populations of osteoblasts and osteoclasts. Much remains to be understood about mechanisms that lead to the formation of lamellae in lamellar bone, but it possible that lamella formation may be linked to behaviours enabled by the discrete nature of osteocytes and their effect on signal propagation.

Our mathematical model has a number of limitations. First, it only considers the evolution of bone length and the propagation of signals in a one-dimensional network. Osteocytes are also assumed to be regularly spaced. While there is some evidence that osteocytes are arranged in layers (Marotti 2000; Ardizzoni 2001), it is not clear what mechanisms may lead to such an arrangement. In our model, we assumed that osteocytes may be stimulated mechanically either by mechanical stress, or by strain energy density. Several works consider other types of mechanical stimulations, such as fluid-flow induced shear stress and dependences upon strain rates (Carter & Beaupré 2001; van Tol et al. 2020a,b). The consideration of other types of mechanical stimulations could lead to yet other behaviours of bone adaptation than those explored in our work. Finally, our model suffers from similar shortcomings as standard mechanostat theories and Wolff's laws, in which full bone resorption occurs under complete disuse, and unbounded bone growth occurs under bending (Levenston et al. 1998; Turner 1999; Skerry 2008; Lerebours 2017). To address these shortcomings, future works may need to account for osteocyte desensitisation and osteocyte network adaptation (Turner 1999; Lerebours & Buenzli 2016; Pauchard & Buenzli 2025).

In conclusion, our mathematical model provides a first model of the regulatory control of the osteocyte network for bone adaptation to mechanical loads. This model illustrates of the importance of accounting for the discrete nature of osteocytes during bone formation and bone resorption.

Acknowledgements

PRB acknowledges support from the Australian Research Council (DP190102545). AM, VJC, and PRB acknowledge support from the Max Planck Queensland Centre for the Materials Science of Extracellular Matrices (MPQC).

Appendix A Osteoblast and osteoclast parameter estimation

A.1 Instantaneous cell generation model

We examine the instantaneous cell generation model when the loading force is increased by 20% at $t = 40$ days, from $F = 0.04$ N to $F = 0.048$ N. For illustration, we assume equal formation velocity v_{f} and resorption velocity v_{r}. Figure 12a shows the evolution the right boundary position $b_+(t)$ over a short period of time following the overload. The force increase at $t = 40$ days leads to a right boundary flux $J_+(t) > J_0$ (Figure 12b) which induces bone formation (Figure 12a). When sufficient bone is formed to create a new osteocyte, this new osteocyte has no signalling molecules initially. The flux J_+ drops to zero (Figure 12b). This immediately leads to bone resorption in the instantaneous cell generation model by Eq (16), which in turn triggers the resorption of the newly formed osteocyte. Since that osteocyte has collected signalling molecules meanwhile, its

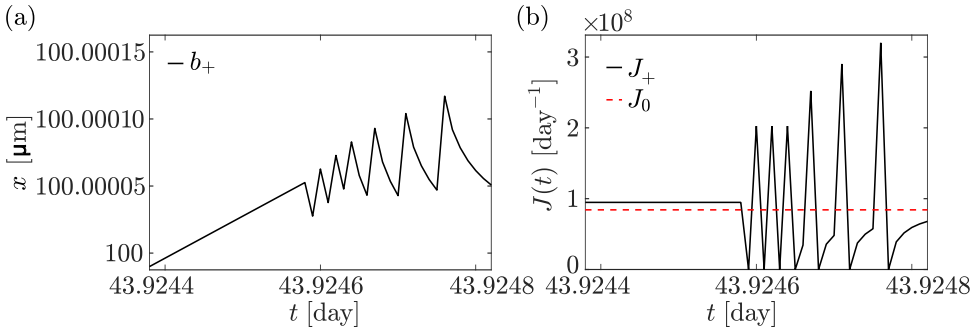

Figure 12 – Overloading the instantaneous cell generation model with a 20 % force increase from $F = 0.04\,\mathrm{N}$ to $F = 0.048\,\mathrm{N}$ at $t = 40\,\mathrm{day}$. (a) Evolution of $i_+\Delta x$ (grey line) and the right boundary position (black line) over time. (b) Evolution of the right boundary flux (black line) over time corresponding to (a), with the reference value J_0 shown (red dashed line). Parameters: $J_0 = 8.42262 \times 10^7\,/\mathrm{day}$, $D = 3200000\,\mu\mathrm{m}^2/\mathrm{day}$, $\Delta t = 10^{-5}\,\mathrm{day}$, $K = 21$, $\overline{L} = 200\,\mu\mathrm{m}$, $\overline{F} = 0.04\,\mathrm{N}$, $\lambda_1 = 11059200/\mathrm{day}$, $\lambda_2 = 320/\mathrm{day}$, and $v_\mathrm{f} = v_\mathrm{r} = 10\,\mu\mathrm{m}/\mathrm{day}$.

resorption frees extra signalling molecules and the flux increases again above J_0, leading to bone formation. The process repeats and leads to unstable oscillations in both the boundary position $b_+(t)$ and the boundary flux $J_+(t)$. Our investigations showed that this behaviour cannot be remedied by choosing different values of v_f and v_r. Such fast responses of the model to changes in $J_+(t)$ are biologically unreasonable, since populations of osteoblasts and osteoclasts take time to generate and to eliminate.

A.2 Differential cell generation model

Compared to the instantaneous cell generation model, the differential cell generation model provides a more controlled response to overload by regulating boundary motion through the gradual accumulation or elimination of osteoblasts and osteoblasts.

Oscillations in boundary positions may still occur in the differential cell generation model. However, unlike in the instantaneous cell generation model, these oscillations remain stable. Figure 13 presents the evolution of the right boundary $b_+(t)$, flux $J_+(t)$, and cell populations $\mathrm{Ob}(t)$ and $\mathrm{Oc}(t)$ when the loading force is increased by 20% from $F = 0.04\,\mathrm{N}$ to $F = 0.048\,\mathrm{N}$ at $t = 40\,\mathrm{day}$. Two different parameter regimes are shown. Figure 13(a) corresponds to an underdamped regime where cell elimination is weak. The boundary flux oscillates, leading to oscillations in the boundary position. Figure 13(b) corresponds to an overdamped regime, where cell elimination is strong. In this regime, there are no oscillations in the boundary position.

Some insights into when the parameters are in an underdamped regime and when they are in an overdamped regime can be gained when the parameters satisfy some symmetry conditions, as detailed in Section A.2.1.

A.2.1 Criterion for overdamped regime

The numerical simulations presented in Figure 13 suggest that the cell elimination rate in Eqs. (19) and (20) helps control oscillations in the boundary position and flux. To understand why, we seek a mathematical expression that characterises the overdamped regime under further assumptions on parameter values in which bone formation and bone resorption parameters have similar values. While this is not what is assumed in simulations presented in our paper, the analysis made under these assumptions still provides a good indication of how parameters affect

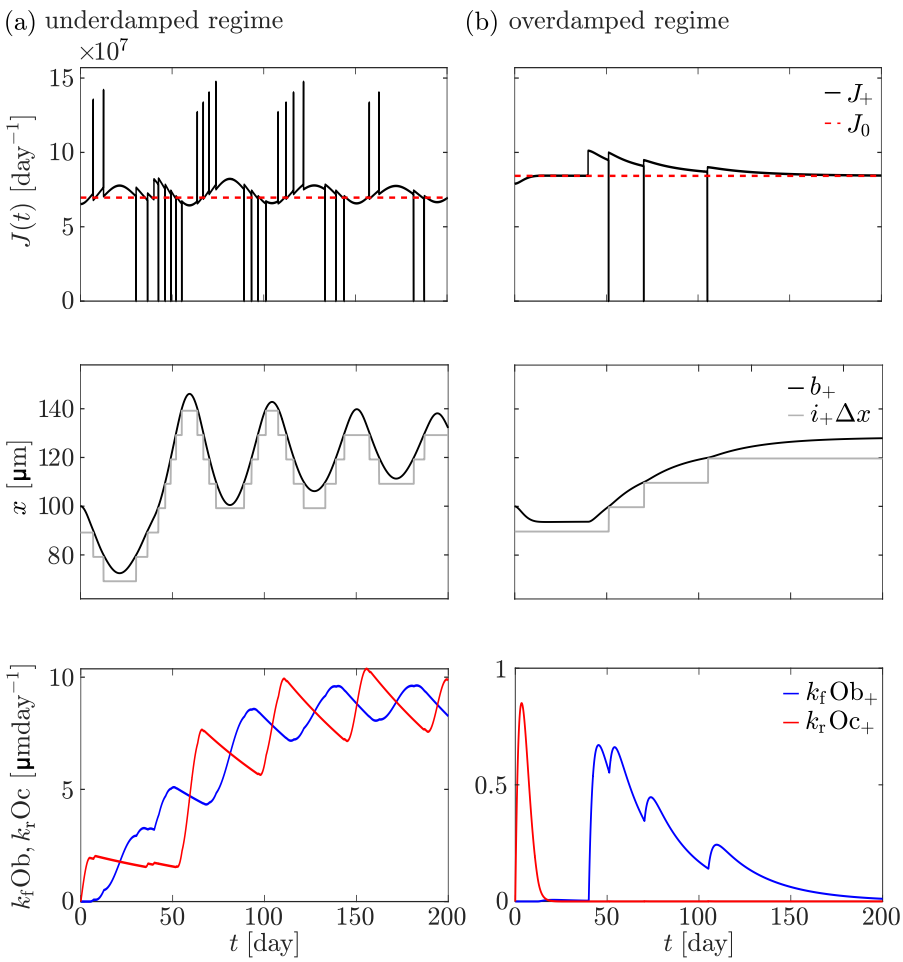

Figure 13 – Overloading the differential cell generation model with a 20 % force increase from $F = 0.04\,\mathrm{N}$ to $F = 0.048\,\mathrm{N}$ at $t = 40\,\mathrm{day}$. Each column includes plots of evolution of the right boundary flux (black line) over time with the reference value J_0 shown (red dashed line), evolution of $i_+\Delta x$ (grey line) and the right boundary position (black line) over time, and speed of osteoblast-driven (blue line) and osteoclast-driven (red line) boundary movement at the right boundary over time. (a) Underdamped regime with $A_{\mathrm{Ob}} = A_{\mathrm{Oc}} = 0.01\,/\mathrm{day}$. (b) Overdamped regime with $A_{\mathrm{Ob}} = A_{\mathrm{Oc}} = 0.5\,/\mathrm{day}$. Parameters: $J_0 = 8.42262 \times 10^7\,/\mathrm{day}$, $D = 3200000\,\mu\mathrm{m}^2/\mathrm{day}$, $\Delta t = 10^{-5}\,\mathrm{day}$, $K = 21$, $\overline{L} = 200\,\mu\mathrm{m}$, $\overline{F} = 0.04\,\mathrm{N}$, $\lambda_1 = 11059200/\mathrm{day}$, $\lambda_2 = 320/\mathrm{day}$, $\alpha_{\mathrm{Ob}} = 0.04\,/\mathrm{day}$, $\alpha_{\mathrm{Oc}} = 0.2\,/\mathrm{day}$, and $k_{\mathrm{f}} = k_{\mathrm{r}} = 50\,\mathrm{day}$.

oscillation damping.

Since the loading force and initial condition are symmetric, $\mathrm{Ob}_+(t) = \mathrm{Ob}_-(t)$ and $\mathrm{Oc}_+(t) = \mathrm{Oc}_-(t)$. The evolution of network length over time is governed by:

$$\frac{\mathrm{d}L}{\mathrm{d}t} = \frac{\mathrm{d}}{\mathrm{d}t}(b_+ - b_-) = 2(k_{\mathrm{f}}\mathrm{Ob}_+ - k_{\mathrm{r}}\mathrm{Oc}_+). \tag{45}$$

Differentiating with respect to time and using Eqs (17)–(18), we have

$$\frac{\mathrm{d}^2L}{\mathrm{d}t^2} = 2\left(k_{\mathrm{f}}\alpha_{\mathrm{Ob}}\left[\frac{J_+(L) - J_0}{J_0}\right]_+ - k_{\mathrm{r}}\alpha_{\mathrm{Oc}}\left[\frac{J_0 - J_+(L)}{J_0}\right]_+\right) - 2(k_{\mathrm{f}}A_{\mathrm{Ob}}\mathrm{Ob}_+ - k_{\mathrm{r}}A_{\mathrm{Oc}}\mathrm{Oc}_+), \tag{46}$$

where we wrote the dependence of J_+ upon L explicitly. To simplify the analysis of the behaviour

of Eq. (46), we now assume that

$$2k_{\mathrm{f}}\alpha_{\mathrm{Ob}} = 2k_{\mathrm{r}}\alpha_{\mathrm{Oc}} = K \tag{47}$$

$$A_{\mathrm{Ob}} = A_{\mathrm{Oc}} = A. \tag{48}$$

Since $[x]_+ - [-x]_+ = x$ for any value x, Eq. (46) becomes

$$\begin{aligned}\frac{\mathrm{d}^2 L}{\mathrm{d}t^2} &= K\left(\frac{J_+(L)-J_0}{J_0}\right) - 2A(k_{\mathrm{f}}\mathrm{Ob}_+ - k_{\mathrm{r}}\mathrm{Oc}_+) \\ &= K\left(\frac{J_+(L)-J_0}{J_0}\right) - A\frac{\mathrm{d}L}{\mathrm{d}t},\end{aligned} \tag{49}$$

where we used Eq. (45) for the second equality. Equation (49) corresponds to the evolution equation of a nonlinear damped oscillator. Its oscillatory behaviour around the homeostatic steady state $L = \overline{L}$ when $F = \overline{F}$ can be assessed by linearising $J_+(L)$ about $\overline{L}$. For this, we assume that $J_+(L)$ can be approximated by the steady-state expression in Eq. (26) (since molecule propagation dynamics is much faster than bone length changes). With Eq. (31), we can write, when $F = \overline{F}$,

$$J_+(L) \approx J_0 \frac{\overline{L}}{L} \frac{\tanh\left(\frac{L}{2\Lambda_D}\right)}{\tanh\left(\frac{\overline{L}}{2\Lambda_D}\right)} \tag{50}$$

Linearising Eq. (50) about $\overline{L}$ gives

$$J_+(L) \approx J_0\left[1 - \left(\frac{1}{\overline{L}} - \frac{\mathrm{sech}(\overline{L}/\Lambda_D)}{\Lambda_D}\right)(L-\overline{L})\right],$$

so that linearising Eq. (49) about $L = \overline{L}$ gives

$$\frac{\mathrm{d}^2(L-\overline{L})}{\mathrm{d}t^2} = -K\left(\frac{1}{\overline{L}} - \frac{\mathrm{sech}(\overline{L}/\Lambda_D)}{\Lambda_D}\right)(L-\overline{L}) - A\frac{\mathrm{d}(L-\overline{L})}{\mathrm{d}t} \tag{51}$$

Equation (51) is the evolution equation of a damped harmonic oscillator. Its overdamped regime is obtained when

$$A^2 > 4K\left(\frac{1}{\overline{L}} - \frac{\mathrm{sech}(\overline{L}/\Lambda_D)}{\Lambda_D}\right). \tag{52}$$

References

Adachi T, Kameo Y and Hojo M (2010) Trabecular bone remodelling simulation considering osteocytic response to fluid-induced shear stress. *Phil Trans R Soc A* 368:2669–2682; https://doi.org/10.1098/rsta.2010.0073

Adachi T and Kameo Y (2018) Computational biomechanics of bone adaptation by remodeling. In *Multiscale Mechanobiology of Bone Remodeling and Adaptation* 231–257; https://doi.org/10.1007/978-3-319-58845-2_5

Ardizzoni A (2001) Osteocyte lacunar size–lamellar thickness relationships in human secondary osteons. *Bone* 28:215–219.

Barrat A, Barthélemy M, Vespignani A (2005) The effects of spatial constraints on the evolution of weighted complex networks. *Journal of Statistical Mechanics: Theory and Experiment* 2005: P05003; https://doi.org/10.1088/1742-5468/2005/05/P05003

Bertram JEA, Swartz SM (1991) The 'law of bone transformation': A case of the crying Wolff? *Biol Rev* 66:242–273

Bonewald LF (2011) The amazing osteocyte, *J Bone Miner Res* 26:229–238

Buenzli PR and Sims NA (2015) Quantifying the osteocyte network in the human skeleton. *Bone* 75:144–150; https://doi.org/10.1016/j.bone.2015.02.016

Carriero A et al. (2018) Spatial relationship between bone formation and mechanical stimulus within cortical bone: combining 3D fluorochrome mapping and poroelastic finite element modelling. *Bone Reports* 8:72–80; https://doi.org/10.1016/j.bonr.2018.02.003

Carter DR, Beaupré GS (2001) *Skeletal Function and Form. Mechanobiology of skeletal development, aging, and regeneration* (Cambridge University Press)

Chen JH, Liu C, You L, Simmons CA (2010) Boning up on Wolff's Law: mechanical regulation of the cells that make and maintain bone. *Journal of Biomechanics* 43:108–118; https://doi.org/10.1016/j.jbiomech.2009.09.016

Cheong VS, Kadirkamanathan V, Dall'Ara E (2021) The role of the loading condition in predictions of bone adaptation in a mouse tibial loading model. *Frontiers in Bioengineering and Biotechnology* 9:676867; https://doi.org/10.3389/fbioe.2021.676867

Cheong VS et al. (2020) Bone remodelling in the mouse tibia is spatio-temporally modulated by oestrogen deficiency and external mechanical loading: A combined in vivo/in silico study. *Acta Biomaterialia* 116:302–317; https://doi.org/10.1016/j.actbio.2020.09.011

Chou HY, Jagodnik JJ, Müftü S (2008) Predictions of bone remodeling around dental implant systems. *J Biomech* 41:1365–1373; https://doi.org/10.1016/j.jbiomech.2008.01.032

Cowin SE (Ed.) (2001) *Bone Mechanics Handbook*, 2nd Ed. (CRC Press)

Dunstan, CR, Somers MS, and Evans RA (1993) Osteocyte Death and Hip Fracture. *Calcified Tissue International* 53:S113–S117

Fallahnezhad K, Farhoudi H, Oskouei RH, Taylor M (2017) A finite element study on the mechanical response of the head-neck interface of hip implants under realistic forces and moments of daily activities: Part 2. *J Mech Beh Biomed Mat* 77:164–170; http://dx.doi.org/10.1016/j.jmbbm.2017.08.038

Farhoudi H, Fallahnezhad K, Oskouei RH, Taylor M (2017) A finite element study on the mechanical response of the head-neck interface of hip implants under realistic forces and moments of daily activities: Part 1, level walking. *J Mech Beh Biomed Mat* 75:470–476; http://dx.doi.org/10.1016/j.jmbbm.2017.08.012

Ferguson BM, Entezari A, Fang J, Li Q (2022) Optimal placement of fixation system for scaffold-based mandibular reconstruction. *J Mech Beh Biomed Mat* 126:104855; https://doi.org/10.1016/j.jmbbm.2021.104855

Ferretti M and Palumbo C (2021) Static Osteogenesis versus Dynamic Osteogenesis: A Comparison between Two Different Types of Bone formation. *Appl Sci* 11:2025; https://doi.org/10.3390/app11052025

Franz-Odendaal TA, Hall BK, Witten PE (2006) Buried alive: how osteoblasts become osteocytes, *Develop Dyn* 235:176

Frost HM (2003). Bone's Mechanostat: A 2003 Update. *The Anatomical Record Part A: Discoveries in Molecular, Cellular, and Evolutionary Biology* 275A:1081–1101

Hernandez CJ, Beaupré GS, and Carter DR (2000) A Model of Mechanobiologic and Metabolic Influences on Bone Adaptation. *Journal of Rehabilitation Research and Development* 37:235–244

Hu Q, Zhang XD (2024) Fundamental patterns of signal propagation in complex networks. *Chaos: An Interdisciplinary Journal of Nonlinear Science* 34:013149; https://doi.org/

10.1063/5.0180450
Huiskes R, Weinans H, Grootenboer HJ et al. (1987) Adaptive bone-remodeling theory applied to prosthetic-design analysis. *J Biomech* 20:1135–1150
Huiskes R et al. (2000) Effects of mechanical forces on maintenance and adaptation of form in trabecular bone. *Nature* 405:704–706; https://doi.org/10.1038/35015116
Jang IG and Kim IY (2010) Computational simulation of simultaneous cortical and trabecular bone change in human proximal femur during bone remodeling. *J Biomech* 43:294–301
Jörg DJ, Fuertinger DH, Cherif A, Bushinsky DA, Mermelstein A, Raimann JG, Kotanko P (2022) Modeling osteoporosis to design and optimize pharmacological therapies comprising multiple drug types. *eLife* 11:e76228; https://doi.org/10.7554/eLife.76228
Kim SH et al. (2007) ERK 1/2 activation in enhanced osteogenesis of human mesenchymal stem cells in poly (lactic-glycolic acid) by cyclic hydrostatic pressure. *Journal of Biomedical Materials Research Part A* 80:826–836; https://doi.org/10.1002/jbm.a.30945
Klein-Nulend J, Bacabac RG (2012) Bone adaptation and regeneration? New developments. *International Journal of Modern Physics: Conference Series* 17:34–43; https://doi.org/10.1142/S201019451200791X
Knothe Tate ML, Steck R, Forwood MR, Niederer P (2000) In vivo demonstration of load-induced fluid flow in the rat tibia and its potential implications for processes associated with functional adaptation. *The Journal of Experimental Biology* 203:2737–2745
Lerebours C & Buenzli PR (2016) Towards a cell-based mechanostat theory of bone: the need to account for osteocyte desensitisation and osteocyte replacement. *J Biomech* 49:2600–2606; http://dx.doi.org/10.1016/j.jbiomech.2016.05.012
Lerebours C (2017) *Mechanical adaptation in dynamic bone tissues*, PhD thesis, Monash University, Australia; https://doi.org/10.4225/03/5a03a4a338de4
Levenston ME, Beaupré GS, Carter DR (1998) Loading mode interactions in simulations of long bone cross-sectional adaptation. *Computer Methods in Biomechanics and Biomedical Engineering* 1:303–319; https://doi.org/10.1080/01495739808936709
Li Y, Johnston ST, Buenzli PR, van Heijster P, Simpson MJ (2022) Extinction of bistable populations is affected by the shape of their initial spatial distribution. *Bull Math Bio* 84:21; https://doi.org/10.1007/s11538-021-00974-5
Maldonado S et al. (2006) Mathematical modeling and analysis of force induced bone growth. In *2006 International Conference of the IEEE Engineering in Medicine and Biology Society* 3154–3157; https://doi.org/10.1109/IEMBS.2006.260532
Manolagas SC, Parfitt AM (2013) For whom the bell tolls: distress signals from long-lived osteocytes and the pathogenesis of metabolic bone diseases. *Bone* 54:272–278; https://doi.org/10.1016/j.bone.2012.09.017
Marotti G (1993) A new theory of bone lamellation. *Calcif Tissue Int* 53(Suppl 1):S47–S56
Marotti G (2000) The osteocyte as a wiring transmission system. *J Muskuloskel Neuron Interact* 1:133
Martin RB (2003) Fatigue damage, remodeling, and the minimization of skeletal weight. *J Theor Biol* 220:271–276
Martin RB, Burr DB, Sharkey NA (1998) *Skeletal Tissue Mechanics* (Springer); https://doi.org/10.1007/978-1-4939-3002-9
Masuda N, Porter MA, Lambiotte R (2017) Random walks and diffusion on networks. *Physics reports* 716:1–58; https://doi.org/10.1016/j.physrep.2017.07.007
McGarry JG, Klein-Nulend J, Mullender MG, Prendergast PJ (2005) A comparison of strain and fluid shear stress in stimulating bone cell responses - A computational and experimental study. *The FASEB Journal* 19:1–22; https://doi.org/10.1096/fj.04-2210fje

McNamara LM, Van der Linden JC, Weinans H, Prendergast PJ (2006) Stress-concentrating effect of resorption lacunae in trabecular bone. *Journal of Biomechanics*, 39:734–741; https://doi.org/10.1016/j.jbiomech.2004.12.027

Mehrpooya A, Challis VJ, Buenzli PR (2024) Random walk models for the propagation of signalling molecules in one-dimensional spatial networks and their continuum limit. *Proceeding of the Royal Society A* 480:20230906; https://doi.org/10.1098/rspa.2023.0906

Moriishi T et al. (2012) Osteocyte Network; a Negative Regulatory System for Bone Mass Augmented by the Induction of Rankl in Osteoblasts and Sost in Osteocytes at Unloading. *PLoSONE* 7:e40143; https://doi.org/10.1371/journal.pone.0040143.t001

Mullender MG and Huiskes R (1995) Proposal for the Regulatory Mechanism of Wolff's Law. *J Orthop Res* 13:503–512

Mullender MG, van der Meer DD, Huiskes R, and Lips P (1996) Osteocyte Density Changes in Aging and Osteoporosis. *Bone* 18:109–13

Nakashima T et al. (2011) Evidence for osteocyte regulation of bone homeostasis through RANKL expression. *Nat Medicine* 17:1231–1234; https://doi.org/10.1038/nm.2452

Norvell SM et al. (2004) Fluid shear stress induces β-catenin signaling in osteoblasts. *Calcified Tissue International* 75:396–404; https://doi.org/10.1007/s00223-004-0213-y

van Oers RFM, Ruimerman R, Tanck E, Hilbers PAJ, Huiskes R (2008) A unified theory for osteonal and hemi-osteonal remodeling. *Bone* 42:250–259; https://doi.org/10.1016/j.bone.2007.10.009

Oliviero S et al. (2021) Non-invasive prediction of the mouse tibia mechanical properties from microCT images: comparison between different finite element models. *Biomechanics and Modeling in Mechanobiology* 20:941–955; https://doi.org/10.1007/s10237-021-01422-y

Palumbo C, Ferretti M (2021) The Osteocyte: From "Prisoner" to "Orchestrator". *J Funct Morphol Kinesiol* 6:28; https://doi.org/10.3390/jfmk6010028

Peyroteo MMA, Belinha J, Natal Jorge RM (2021) A mathematical biomechanical model for bone remodeling integrated with a radial point interpolating meshless method. *Computers in Biology and Medicine* 129:104170; https://doi.org/10.1016/j.compbiomed.2020.104170

Peyroteo MMA, Belinha J, Natal Jorge, RM (2021) Load adaptation through bone remodeling: a mechanobiological model coupled with the finite element method. *Biomechanics and Modeling in Mechanobiology* 20:1495–1507; https://doi.org/10.1007/s10237-021-01458-0

Prasad J, Goyal A (2019) An invertible mathematical model of cortical bone's adaptation to mechanical loading. *Scientific Reports* 9:5890; https://doi.org/10.1038/s41598-019-42378-5

Pauchard Y and Buenzli PR (2025) The "osteostat": a theory of bone mechanosensing and setpoint adaptation based on osteocytes. In preparation.

Qin L et al. (2020) The osteocyte. *The International Journal of Biochemistry & Cell Biology, Bone Research* **8(1)**, 23 (2020) https://doi.org/10.1038/s41413-020-0099-y

Qing H, Bonewald LF (2009) Osteocyte remodeling of the perilacunar and pericanalicular matrix. *International Journal of Oral Science* 1:59–65

Qiu SD, Rao S, Palnitkar S, and Parfitt AM (2002) Relationships between Osteocyte Density and Bone Formation Rate in Human Cancellous Bone. *Bone* 31:709–11

Qiu S, Rao DS, Palnitkar S, and Parfitt AM (2002) Age and Distance from the Surface but Not Menopause Reduce Osteocyte Density in Human Cancellous Bone. *Bone* 31:313–18

Robinson JA et al. (2006) Wnt/β-catenin signaling is a normal physiological response to

mechanical loading in bone. *Journal of Biological Chemistry* 281:31720–31728; https://doi.org/10.1074/jbc.M602308200

Robling AG, Castillo AB, Turner CH (2006) Biomechanical and molecular regulation of bone remodeling. *Annual Review of Biomedical Engineering* 8:455–498; https://doi.org/10.1146/annurev.bioeng.8.061505.095721

Robling AG, Turner CH (2009) Mechanical signaling for bone modeling and remodeling. *Critical Reviews in Eukaryotic Gene Expression* 19

Rosa N et al. (2015) From mechanical stimulus to bone formation: A review. *Medical Engineering and Physics* 37:719–728; http://dx.doi.org/10.1016/j.medengphy.2015.05.015

Ryser MD, Nigam N, Komarova SV (2009) Mathematical Modeling of Spatio-Temporal Dynamics of a Single Bone Multicellular Unit. *J Bone Miner Res* 24:860–870; https://doi.org10.1359/JBMR.081229

Schulte FA, Zwahlen A, Lambers FM, et al. (2013) Strain-adaptive in silico modeling of bone adaptation–A computer simulation validated by in vivo micro-computed tomography data. *Bone* 52:485–492; https://dx.doi.org/10.1016/j.bone.2012.09.008

Simpson MJ, Landman KA, Hughes BD, Fernando AE (2010) A model for mesoscale patterns in motile populations. *Physica A* 389:1412–1424; https://dx.doi.org/10.1016/j.physa.2009.12.010

Skerry TM (2008) The response of bone to mechanical loading and disuse: Fundamental principles and influences on osteoblast/osteocyte homeostasis. *Archives Biochem Biophys* 472:117–123.

Smotrova E, Li S, Silberschmidt VV (2022) Mechanoregulated trabecular bone adaptation: progress report on in silico approaches. *Biomaterials and Biosystems* 7:100058; https://doi.org/10.1016/j.bbiosy.2022.100058

Tate MLK et al. (2004) Molecular mechanosensors in osteocytes. *Bone Research* 36:1–8; https://doi.org/10.1016/S1357-2725(03)00241-3

Taylor-King JP et al. (2020) Modeling osteocyte network formation: healthy and cancerous environments. *Frontiers in Bioengineering and Biotechnology* 8:757; https://doi.org/10.3389/fbioe.2020.00757

Tiede-Lewis LM and Dallas SM (2019) Changes in the Osteocyte Lacunocanalicular Network with Aging. *Bone* 122:101–113.

Van Tol AF et al. (2020) The mechanoresponse of bone is closely related to the osteocyte lacunocanalicular network architecture. *Proceedings of the National Academy of Sciences* 117:32251–32259; https://doi.org/10.1073/pnas.2011504117

Van Tol AF, Repp F, Chen J, Roschger P, Berzlanovich A, Gruber GM, Fratzl P, Weinkamer R (2020) Network architecture strongly influences the fluid flow pattern through the lacunocanalicular network in human osteons. *Biomechanics and Modeling in Mechanobiology* 19:823–840; https://doi.org/10.1007/s10237-019-01250-1

Turner CH and Forwood MR (1995) What role does the osteocyte network play in bone adaptation? *Bone* 16:283–285

Turner CH (1999) Toward a mathematical description of bone biology: The principle of cellular commodation. *Calcif Tissue Int* 65:466–471

VandenHeuvel DJ, Buenzli PR, Simpson MJ (2024) Pushing coarse-grained models beyond the continuum limit using equation learning. *Proc Roy Soc A* 480:20230619; https://doi.org/10.1098/rspa.2023.0619

Vashishth D, Verborgt O, Divine G, Schaffler MB, and Fyhrie DP (2000) Decline in osteocyte lacunar density in human cortical bone is associated with accumulation of microcracks with

age. *Bone* 26:375–380

Vashishth D (2007) Hierarchy of bone microdamage at multiple length scales. *International Journal of Fatigue* 29:1024–1033 (2007) https://doi.org/10.1016/j.ijfatigue.2006.09.010

Verbruggen SW, Vaughan TJ, McNamara LM (2014) Fluid flow in the osteocyte mechanical environment: a fluid-structure interaction approach. *Biomechanics and Modeling in Mechanobiology* 13:85–97; https://doi.org/10.1007/s10237-013-0487-y

Vilone D, Vespignani A, Castellano C (2002) Ordering phase transition in the one-dimensional Axelrod model. *The European Physical Journal B-Condensed Matter and Complex Systems* 30:399–406; https://doi.org/10.1140/epjb/e2002-00395-2

Wan B, Yoda N, Zheng K, Zhang Z, Wu C, Clark J, Sasaki K, Swain M, Li Q (2022) On interaction between fatigue of reconstruction plate and time-dependent bone remodeling. *J Mech Beh Biomed Mat* 136:105483; https://doi.org/10.1016/j.jmbbm.2022.105483

Wang L, Shi Q, Cai Y, et al. (2020) Mechanical-chemical coupled modeling of bone regeneration within a biodegradable pplymer scaffold loaded with VEGF. *Biomech Model Mechanobiol* 19:2285–2306

Wang L et al. (2022) Mechanical regulation of bone remodeling. *Bone research* 10:16; https://doi.org/10.1038/s41413-022-00190-4

Wang Y, Wang L, Soro N, Buenzli PR, Li Z, Green N, Tetsworth K, Erbulut D (2023) Bone ingrowth simulation within the hexanoid, a novel scaffold design. *3D Printing and additive manufactoring*; https://doi.org/10.1089/3dp.2023.0113

Weinkamer R, Kollmannsberger P, Fratzl P (2019) Towards a connectomic description of the osteocyte lacunocanalicular network in bone. *Current Osteoporosis Reports* 17:186–194; https://doi.org/10.1007/s11914-019-00515-z

Weyts FA et al. (2003) Mechanical control of human osteoblast apoptosis and proliferation in relation to differentiation. *Calcified Tissue International* 72:505–512; https://doi.org/10.1007/s00223-002-2027-0

Xiong J et al. (2011) Matrix-embedded cells control osteoclast formation. *Nature Medicine* 17:1235–1241; https://doi.org/10.1038/nm.2448